Effective Density Derived from Laboratory Measurements of the Vapor

Growth Rates of Small Ice Crystals at -65 to -40°C

- Gwenore F. Pokrifka, Alfred M. Moyle, and Jerry Y. Harrington
- Department of Meteorology and Atmospheric Science, The Pennsylvania State University,
- University Park, Pennsylvania

6 Corresponding author: Gwenore F. Pokrifka, gfp5025@psu.edu

- ABSTRACT: An electrodynamic levitation thermal-gradient diffusion chamber was used to grow
- ₈ 268 individual, small ice particles (initial radii of 8 26μ m) from the vapor, at temperatures
- ₉ ranging from -65 to -40°C, and supersaturations up to liquid saturation. Growth limited by
- attachment kinetics was frequently measured at low supersaturation, as shown in prior work. At
- high supersaturation enhanced growth was measured, likely due to the development of branches
- and hollowed facets.
- The effects of branching and hollowing on particle growth are often treated with an effective density
- ρ_{eff} . We fit the measured time-series with two different models to estimate size-dependent ρ_{eff}
- values: The first model decreases ρ_{eff} to an asymptotic deposition density ρ_{dep} , and the second
- models ρ_{eff} by a power-law with exponent P. Both methods produce similar results, though the
- fits with ρ_{dep} typically have lower relative errors. The fit results do not correspond well with
- models of isometric or planar single-crystalline growth. While single-crystalline columnar crystals
- 19 correspond to some of the highest growth rates, a newly constructed geometric model of budding
- 20 rosette crystals produces the best match with the growth data.
- The relative frequency of occurrence of ρ_{dep} and P- values show a clear dependence on ice
- supersaturation normalized to liquid saturation. We use these relative frequencies of ho_{dep} and
- ²³ P to derive two supersaturation-dependent mass-size relationships suitable for cloud modeling
- 24 applications.

1. Introduction

The early growth of ice in clouds is a challenging problem, and little is known about the shapes 26 and growth rates of small (radius $\lesssim 50 \ \mu m$) ice crystals immediately after nucleation. As a newlynucleated ice particle begins to grow from the vapor, facets develop on the crystal, altering its 28 growth rate. The formation and growth of facets, and thus particle shape, is controlled by gas-29 phase vapor diffusion and attachment kinetics. "Attachment kinetics" refers to the set of processes in which vapor molecules adsorb onto and diffuse along the ice surface, until they either desorb 31 or incorporate into the ice. When the ice supersaturation (hereafter "supersaturation", s_i) is high, facet instabilities can lead to the development of branching and hollowing on crystals. Much of the interior surface area of a branched or hollowed particle is "shadowed" and experiences low supersaturation, resulting in slow growth compared to the crystal's extremities that extend further into the vapor field where s_i is higher (Nelson 2001). The extremities then grow rapidly, and it is the resistance to vapor growth on much of the particle due to attachment kinetics that causes the particle to increase in size and mass faster than a solid ice sphere. This is true even for small particles which can become branched and hollowed (Magee et al. 2021). However, no exact method exists to treat such processes.

Due to the effects of attachment kinetics, mass is not added uniformly across a growing ice particle, otherwise it would remain spherical. Thus, to model the growth of an ice particle, one must make some assumptions regarding the distribution of added mass. For example, the basic planar or columnar habit of a crystal may be approximated as a spheroid (Chen and Lamb 1994), or simply as a sphere. But in each case, any "complexity" in the crystal such as branching, hollowing, and non-spherical habit is treated with an "effective" density that is reduced from the bulk ice density (~920 kg m⁻³).

A variety of techniques have been used to estimate the effective densities of ice particles. One approach is to acquire in-situ estimates of cloud particle sizes and masses (Heymsfield and Iaquinta 2000; Baker and Lawson 2006; Erfani and Mitchell 2016). While in-situ observations have the benefit of examining entire populations of particles, their studies typically cannot determine the density of small crystals. The results from Cotton et al. (2013) are an exception, suggesting that particles with radii less than 35 μ m are characterized by a constant effective density of 700 kg m⁻³. Limits on the optical resolution of airborne probes can add uncertainty to the shapes and sizes of

small particles, however, Erfani and Mitchell (2016) estimated effective densities of particles with maximum dimensions down to 20 μ m using a cloud particle imager. Further uncertainty arises 56 from the fact that two-dimensional projections of particles can correspond to numerous particle 57 orientations and three-dimensional geometries (Dunnavan and Jiang 2019; Dunnavan et al. 2019). Another method of estimating the effective density of ice is from ground-based observations of 59 precipitating snowflakes (Muramoto et al. 1995; Brandes et al. 2007; Rees et al. 2021; Leinonen 60 et al. 2021). One benefit of ground-based versus aircraft observations is that the ice particles can be imaged more than once and from multiple directions. For example, a Multi-Angle Snowflake Camera (MASC, Garrett et al. 2015) utilizes multiple camera views to reliably record a snowflake's three-dimensional geometry (Dunnavan et al. 2019; Rees et al. 2021; Leinonen et al. 2021). However, the effective densities derived from ground-based observations of large (radius $\gtrsim 0.5$ mm) snowflakes are not applicable to the small crystals (radius $< 100 \mu m$). Both aircraft and ground-66 based methods only have instantaneous views of particles, and thus cannot provide information on 67 how effective density changes in time. Yet the time variation of particle mass and size is required to evaluate and improve growth models. 69

Time variation of the effective ice density may be derived from laboratory measurements. Prior 70 experiments have grown ice particles in cloud chambers (Fukuta 1969; Ryan et al. 1974, 1976; Weitzel et al. 2020) and wind tunnels (Matsuo and Fukuta 1987; Takahashi and Fukuta 1988; 72 Takahashi et al. 1991). Wind tunnel experiments suspend crystals for tens of minutes and show that 73 effective densities can decline substantially and rapidly, particularly in pronounced habit regimes (Fukuta and Takahashi 1999). However, all of the prior laboratory measurements of effective density known to the authors were at temperatures (T) higher than -25°C. Polycrystalline ice is more likely to form as T decreases (Parungo and Weickmann 1973; Bacon et al. 2003; Bailey and 77 Hallett 2004) and polycrystals can have substantially lower effective densities than single-crystals (Ryan et al. 1976). Unfortunately, no prior time-series measurements of the growth of small ice 79 crystals exist at low temperatures and high supersaturation. Without such measurements, it is not 80 possible to assess model-generated growth rates, even those derived from instantaneous in-situ observations.

We address this lack of data by presenting results from experiments using small crystals grown in a levitation thermal diffusion chamber at $T < -40^{\circ}$ C. These experiments are used to estimate

effective densities for vapor growth. In the following sections, we describe the experimental design and the crystal growth model used to fit the experimental data. In §4 and 5 we estimate effective densities from the data and use a newly-developed budding rosette model to interpret the data. In §6, two parameterizations of effective-density-size, and therefore, mass-size relationships are derived. These parameterizations link laboratory-determined growth rates to the effective density, therefore allowing the use of measured growth rates in cloud models. We end in §7 with a discussion and summary of our findings.

2. Levitation diffusion chamber ice growth experiments

Our experiments involve growing small (initial radius r_0 of 8 - 26 μ m and equivalent-mass 93 spherical radius $r_s < 40 \ \mu \text{m}$) ice particles inside the Button Electrode Levitation (BEL) thermal-94 gradient diffusion chamber. The chamber is described in detail by Harrison et al. (2016), so we will discuss it only briefly here. The BEL chamber consists of parallel copper plates at the top and bottom, which are separated by a plastic ring 1.27 cm tall and 10.2 cm in diameter. The aspect ratio of 8:1 is sufficiently large so that wall effects are minimized (Elliott 1971). The plate temperatures are controlled independently, and the bottom plate has a lower temperature for thermal stability. Water vapor is supplied by ice-covered filter paper that is affixed to the interior plate surfaces. There are holes in the filter paper on the top plate for four button electrodes and 101 an opening through which droplets are introduced to the chamber. Simulations and measurements 102 reveal that the supersaturation at the center of the chamber may be approximated with diffusion chamber theory (Pokrifka et al. 2020), where the supersaturation is controlled by the difference in 104 the plate temperatures. 105

Charged liquid water droplets are launched into the BEL chamber. The droplets quickly freeze and are levitated by an opposing direct current voltage applied to the bottom plate, and they are stabilized horizontally by an alternating current on the upper electrodes. The charge applied to the ice particles is less than that which could cause electrically enhanced growth (Bacon et al. 2003; Davis 2010; Harrison et al. 2016). During an experiment, the ice particle grows from the vapor, increasing the voltage necessary for levitation. Stable levitation is maintained by software that automatically adjusts the bottom-plate voltage, and records the time-series thereof at 1 Hz. The measured voltage is then normalized by its value at the beginning of the experiment. That

normalization is equivalent to the mass ratio, $m_r = m/m_0$, where m is the particle's mass and m_0 is its mass at the beginning of the experiment. We determine m_0 by illuminating the particle 115 with a helium-neon laser and match the resulting diffraction patterns to Mie theory, which gives 116 the initial spherical radius (r_0) . As the particle grows, the diffraction patterns gradually become disordered, indicating that the particle is no longer spherical. Beyond the initial time, no further 118 size information is directly measured; it must instead be inferred from the mass ratio time-series. 119 The water used in these experiments is either pure high-pressure liquid chromatography (HPLC) 120 water for homogeneous nucleation (177 experiments) or a 0.2 g L⁻¹ mixture of the bionucleant 121 Snomax® in HPLC water (following Harrison et al. 2016) for heterogeneous nucleation (91 exper-122 iments). However, the key results of this study do not show any significant nucleation dependence 123 (i.e., the presence or lack of ice nucleating particles), thus we will be presenting them in aggregate. 124 Experiments were conducted at atmospheric pressure (~ 970 hPa) with conditions that have con-125 stant temperatures ranging from -65 to -40°C and supersaturations from ; 1% to liquid saturation. 126 These conditions cover lower T and higher s_i than previous experiments with the BEL chamber (Harrison et al. 2016; Pokrifka et al. 2020), which used T between -45 and -30°C. For the present ex-128 periments, the device has been upgraded such that the copper plates are now cooled using methanol, 129 which is sealed into its housing with fluorosilicone gaskets, instead of Syltherm™ coolant sealed with Buna-N gaskets. This modification allows the plates to be cooled to $\sim -70^{\circ}$ C without coolant 131 leaks, and the BEL chamber can produce s_i near liquid saturation for temperatures down to -60°. 132 Since high supersaturation requires a large difference between the plate temperatures, achieving liquid saturation at $T < -60^{\circ}$ C would risk causing methanol leaks. Thus, the changes to the device have enabled us to explore experimental conditions where there has been a lack of ice growth data. 135 Next, to interpret the growth data, we compare them to a vapor growth model, as described below.

3. Ice vapor growth model

We analyze the growth data using the Diffusion Surface Kinetics Ice Crystal Evolution (DiSKICE)
model (Harrington et al. 2019). The DiSKICE model can develop the primary habits of faceted
ice with the inclusion of attachment kinetics, and it has been used to successfully interpret prior
laboratory growth data (Harrison et al. 2016; Harrington et al. 2019; Pokrifka et al. 2020). The
DiSKICE model treats the far-field gas-phase diffusion to the ice particle with capacitance theory

and vapor attachment with the theory of faceted growth. The resulting growth equation,

$$\frac{dm}{dt} = 4\pi C(c, a) s_i \rho_{eq} D_{eff}[T, P, \alpha(T, s_i)], \tag{1}$$

is similar in form to the capacitance model, where C(c,a) is the geometric capacitance that depends on the a and c semi-axis lengths, s_i is the ice supersaturation, and ρ_{eq} is the ice equilibrium vapor density. The effective vapor and thermal diffusivity, D_{eff} , includes the influences of attachment kinetics through the deposition coefficient α , which may have different values for the a- and c-semi-dimensions, allowing for the development of the primary habit forms (i.e. plates and columns).

The deposition coefficient is parameterized by Nelson and Baker (1996) as

150

$$\alpha = \left(\frac{s_{surf}}{s_{char}}\right)^{M} tanh \left(\frac{s_{char}}{s_{surf}}\right)^{M}, \tag{2}$$

where s_{surf} is the supersaturation at the particle surface, s_{char} is a characteristic supersaturation, and M is a growth mechanism parameter that ranges from 1 to 30. For example, spiral dislocations are represented by M=1, while $M\geq 10$ is used for step nucleation. Outcroppings of dislocations on the surface likely control the growth of ice following nucleation (Nelson and Knight 1998), producing efficient growth (with $\alpha \geq 0.1$). However, the development of thin crystals with pronounced aspect ratios requires step nucleation, which is far less efficient (Frank 1982). Consequently the growth mode may vary both spatially across a particle (Wood et al. 2001) and temporally (Pokrifka et al. 2020).

At high supersaturation, the deposition coefficients approach unity, therefore attachment kinetics no longer limit growth. But they remain in control of the mass distribution over a particle as branching and/or hollowing occur. Branching and hollowing, and other complexities, are treated through an effective density ρ_{eff} . The DiSKICE model incorporates a time-varying effective density following Chen and Lamb (1994), in which the change in volume V of an enclosing shape about a particle is the change in its mass divided by the density of the deposited ice, or *deposition density* ρ_{dep} . Their Eq. 41 can be written as

$$\frac{dm}{dt} = \frac{d(\rho_{eff}V)}{dt} = \rho_{dep}\frac{dV}{dt}.$$
 (3)

The deposition density is temperature- and supersaturation-dependent, and is determined from measurements (Chen and Lamb 1994). If a crystal formed from a frozen water droplet with an initial density of $\rho_i = 920 \text{ kg m}^{-3}$, integration of the above equation assuming a constant ρ_{dep} gives

$$\rho_{eff}(t) = \rho_i \frac{V_0}{V(t)} + \rho_{dep} \left[1 - \frac{V_0}{V(t)} \right], \tag{4}$$

DiSKICE model decreases in proportion to V^{-1} , or r^{-3} if the enclosing shape is a sphere. It should be noted that such a decrease can be too rapid for larger crystals (Schrom et al. 2020). However, this method is advantageous since the effective density will asymptotically approach ρ_{dep} as the volume increases. Many prior studies have instead characterized ρ_{eff} with a size-dependent power-law (Mitchell 175 1996; Cotton et al. 2013) or polynomial (Erfani and Mitchell 2016). Since we cannot physically

where V_0 is the initial particle volume. Equation 4 clearly shows that the effective density in the

169

Many prior studies have instead characterized ρ_{eff} with a size-dependent power-law (Mitchell 1996; Cotton et al. 2013) or polynomial (Erfani and Mitchell 2016). Since we cannot physically interpret multiple polynomial-fit parameters using a single measured quantity (mass ratio), we also estimate ρ_{eff} with DiSKICE using a power-law,

$$\rho_{eff}(t) = \rho_i \left[\frac{V_0}{V(t)} \right]^{P_V} = \rho_i \left[\frac{r_0}{r(t)} \right]^{P}, \tag{5}$$

where r_0 is the initial radius, r(t) is the enclosing spherical radius at time t, and $P = 3P_V$ is an adjustable parameter determined from best fits to the data. The mass growth rate is then

$$\frac{dm}{dt} = \frac{d(\rho_{eff}V)}{dt} = \rho_i V_0^{P_V} \frac{dV^{1-P_V}}{dt} = (1 - P_V) \cdot \rho_{eff} \frac{dV}{dt}.$$
 (6)

Note that the right-most equation has the same form as that of Eq. 3, except that the deposition density has the form $(1-P_V)\rho_{eff}$, which declines with increasing volume. This form has the disadvantage that ρ_{eff} is not asymptotic and may become nonphysical for large particles. However, the decrease of the deposition density with size leads to an initially slower, and more realistic, decline in ρ_{eff} than Eq. 4 (Schrom et al. 2020). Since both forms of the effective density (Eqs. 4 and 5) are used in parameterizations, we use each to fit the laboratory measurements. Be aware that the ρ_{eff} -values derived from these fits are associated with vapor growth, since the particle geometry is unknown.

4. Measurement Analysis

Ice particles in the size range of our experiments (r_s < 40 μ m) have typically been treated as spheres by prior laboratory measurements (Skrotzki et al. 2013; Harrison et al. 2016) and numerical cloud models (Reisner et al. 1998; Morrison and Milbrandt 2015). Additionally, ice crystal growth is not limited by attachment kinetics when the supersaturation exceeds the characteristic value (s_{char}), which results in large ($\gtrsim 0.1$) deposition coefficients (Eq. 2). For spherical growth in these cases, the DiSKICE model reduces to capacitance theory. Therefore, we compare our measurements to solid spheres grown at the capacitance rate (hereafter "solid spheres").

Note that preparation of the data follows the same procedures as Pokrifka et al. (2020). That is,
we fit the raw mass growth time-series data with cubic functions, then preform any further analysis
on those fits. However, we also use a low-pass filter on the data to illustrate the close fit of the
cubics.

200 a. Effective density fits to growth time-series

Recall that complexity can enhance crystal growth rates. Therefore, ice particles from our 201 experiments with mass growth rates greater than those of solid spheres are candidates to be 202 analyzed for reduced effective densities (ρ_{eff}). While we do not have sufficient visual information to directly measure a particle's morphology in our experiments, the complex habits formed in prior 204 levitation diffusion chamber experiments (see Bacon et al. 2003, their Figs. 5 and 8) indicates that 205 our particles may be treated with an equivalent-diameter sphere and an effective density. Using the DiSKICE model, we simulate the growing crystal while allowing the effective density to decline 207 following either Eq. 4 or 5. We then fit the growth time-series by varying either ρ_{dep} (Eq. 4) or 208 P (Eq. 5) until a minimum in the root-mean-square error is reached. For simplicity, we assume diffusion-limited growth ($\alpha = 1$), which is consistent with frozen droplets initially having many 210 surface dislocations and with the instabilities associated with branching and hollowing (see §3). 211 This assumption may produce growth rates too large for faceted particles (Harrison et al. 2016; 212 Pokrifka et al. 2020), and it is primarily valid for high supersaturations, thus our results are upper estimates of ρ_{eff} . 214

We measured enhanced growth for numerous crystals, and it is therefore not practical to show the time-series for each experiment. Instead, we show characteristic examples of the measured

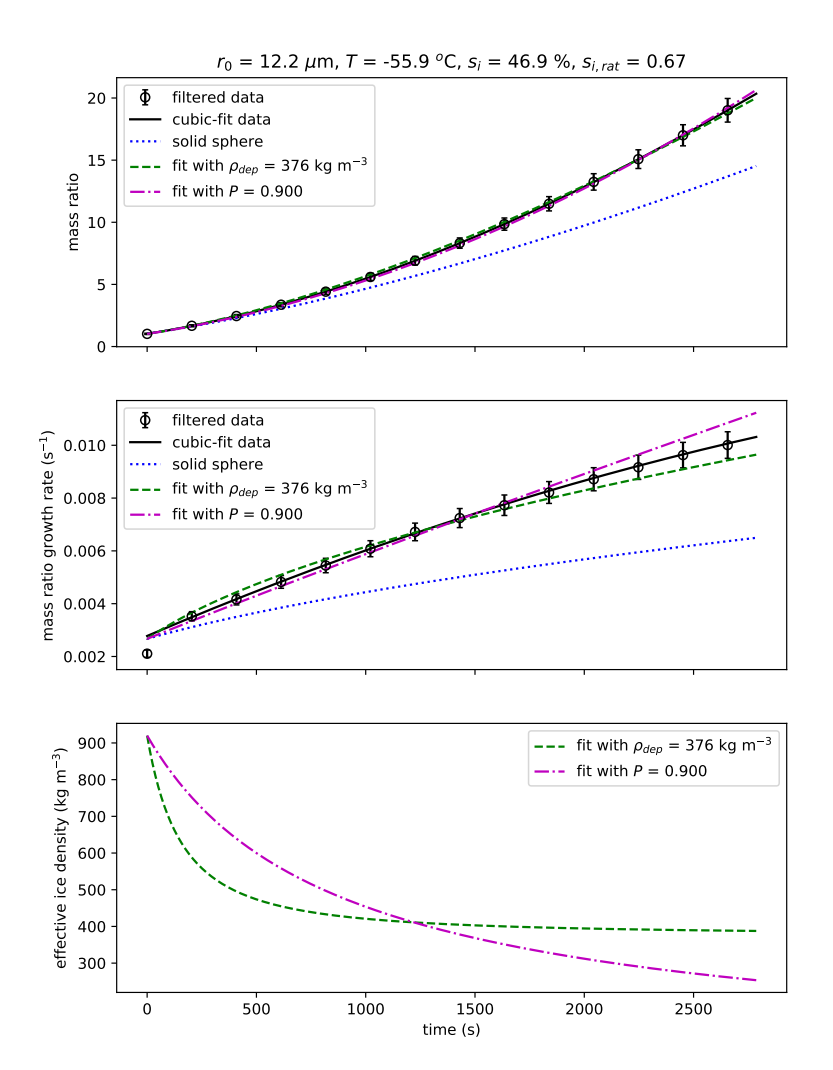


Fig. 1. Representative time-series that is well-fit by both effective density models. The top panel shows the measured mass ratio after low-pass data filtering (black circles, not all points shown), a cubic fit through the data (black curve), a simulated solid sphere with the same initial size (dotted blue curve), an effective density model fit to the data where $\rho_{dep} = 376 \text{ kg m}^{-3}$ (dashed green curve), and an effective density model fit to the data where P = 0.900 (dot-dashed magenta curve). The middle panel shows the mass ratio growth rate $(d(m/m_0)/dt)$. The bottom panel shows the modeled effective density time-series. This experiment had $r_0 = 12.2 \mu \text{m}$, $T = -55.9^{\circ}\text{C}$, $s_i = 46.9\%$, and $s_{i,rat} = 0.67$.

TABLE 1. The following are statistics of the relative errors for the ρ_{dep} and P fitting methods to the mass ratio data. Given are the median error, the mean error, and the standard deviation, along with the maximum and minimum error found among all cases. The percentage of growth experiments with a relative error of less than 5% is also shown.

246

247

248

228

statistic	ρ_{dep}	P
median	1.55%	2.06%
mean	1.92%	2.70%
standard deviation	1.52%	2.21%
maximum	7.95%	10.8%
minimum	0.114%	0.208%
errors < 5%	94.5%	82.4%

growth time-series in Figures 1 and 2, along with model fits to the data. We chose examples that show both accurate fits to the data (Fig. 1), and fits with larger errors (Fig. 2). We find that growth data are well characterized, at a given temperature, by the ratio of the ice supersaturation (s_i) to its value at liquid saturation ($s_{i,max}$, the maximum value expected in a cloud),

We refer to this quantity as the *supersaturation ratio*, which varies between zero and unity (i.e,

$$s_{i,rat} \equiv \frac{s_i}{s_{i,max}}. (7)$$

ice- and liquid-saturation). This ratio provides a common scale for the comparison of data from 229 different temperatures. Both of the presented cases were at high supersaturation ratios of 0.67 and 0.97, respectively. Each case shows that the measured growth (black circles and curves) is 231 greater than predictions using a solid sphere (blue dotted curves). This result is consistent with the 232 development of complex morphology at high s_i . Most cases were similar to the time-series shown in Fig. 1, where the data are accurately modeled 238 by fitting the data with ρ_{dep} (Eq. 4, green dashed curves) or P (Eq. 5, magenta dot-dashed curves). 239 In this case, the particle grew at -55.9°C and 46.9% supersaturation with an initial radius of 12.2 240 μ m, and the best-fits produce values of $\rho_{dep} = 376 \text{ kg m}^{-3}$ and P = 0.90. The relative errors of the fits in Fig. 1 (1.48% and 1.35% for the fits on ρ_{dep} and P, respectively) are near the median for all 242 the experiments (see Table 1), which indicates that both methods consistently produce accurate 243 fits to the growth data.

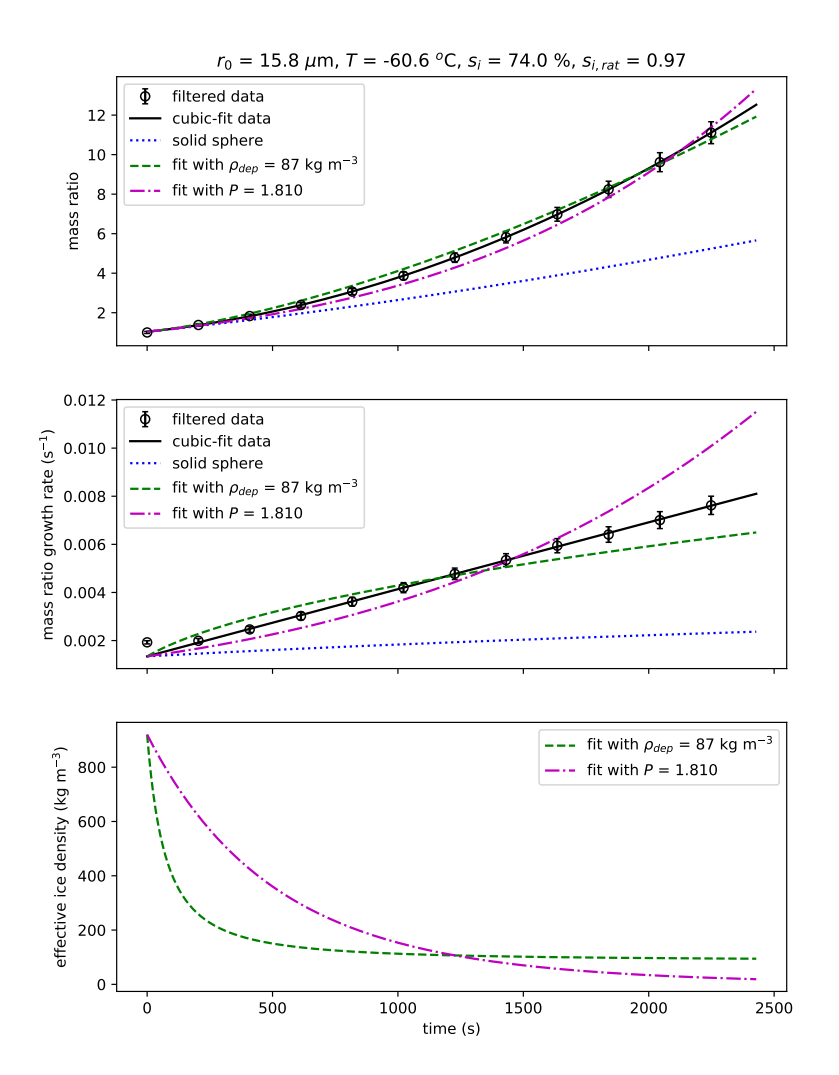


Fig. 2. Representative time-series that is less accurately fit by either effective density model. The panels, points, and linestyles are the same as in Fig. 1, except the dashed green curves are from a fit with $\rho_{dep} = 87$ kg m⁻³ and the dot-dashed magenta curves are from a fit with P = 1.810. This experiment had $r_0 = 15.8\mu$ m, T = -60.6°C, $s_i = 74.0$ %, and $s_{i,rat} = 0.97$.

On the other hand, some of the fitting results had larger errors, where the modeled mass ratios resemble the data, but the growth rates are divergent. A typical example is shown in Fig. 2, for a particle that grew at a temperature of -60.6°C and a supersaturation of 74.0% with an initial radius of 15.8 μ m. The model fit using the deposition density model produces a low value of $\rho_{dep} = 87$

 $_{253}$ kg m⁻³ and the fit with the power-law density produced a best-fit value of P = 1.81, but the relative errors are 4.00% and 5.70%, respectively. Even though the errors are higher in some cases, the effective density models represent the data better than growth of a solid sphere.

Unsurprisingly, the two fitting methods produce different functional forms for the effective density 256 and, therefore, mass growth rate. In Fig. 1, both methods simulate the growth rate comparably 257 well, but the P-fit is noticeably worse in Fig. 2. However, it should be noted that, while the fit 258 with ρ_{dep} typically preformed better than the fit with P (Table 1), that was not always the case. Table 1 further shows that 94.5% of the cases fit with the ρ_{dep} model, and 82.4% of the cases fit 260 with the power-law, had less than 5% errors relative to the data. The mass ratio data themselves are 261 conservatively estimated to have uncertainties of ±5% (Pokrifka et al. 2020). Therefore, nearly all of the best-fit models reproduce the data with sufficient accuracy. In contrast, as the next section 263 will show, the model of a solid sphere underestimates the growth rate with increasing magnitude 264 and frequency as supersaturation increases.

b. Normalized growth rates

Pokrifka et al. (2020) analyzed the inhibition of ice depositional growth due to attachment kinetics using a normalized growth rate, and this methodology is also useful for analyzing growth that is enhanced due to morphological changes. In that work, we defined the normalized growth rate as

$$\dot{m}_{norm} \equiv \frac{\frac{\overline{dm}}{dt}|_{measured}}{4\pi \bar{r_s} D_{eff}}.$$
 (8)

The numerator is the measured growth rate $\frac{dm}{dt}|_{measured}$ averaged for a 1- μ m increase in the equivalent-mass spherical radius (r_s) . This quantity is then normalized by $4\pi \bar{r_s} D_{eff}$, which is the size-increment averaged growth rate of a solid sphere without the supersaturation. Thus, if the particle growing in the diffusion chamber is a solid sphere, then \dot{m}_{norm} would be equal to s_i , and the growth rate data will follow the supersaturation. For growth inhibited by attachment kinetics, the normalized growth rates from the data are less than those of solid spheres (Pokrifka et al. 2020). In the current study, we focus primarily on regimes in which the growth is enhanced.

Figure 3 shows the normalized growth rates for particles in the r_s range of 14 - 15 μ m plotted against the supersaturation ratio (s_i scaled by $s_{i,max}$, Eq. 7). The normalized growth rates have

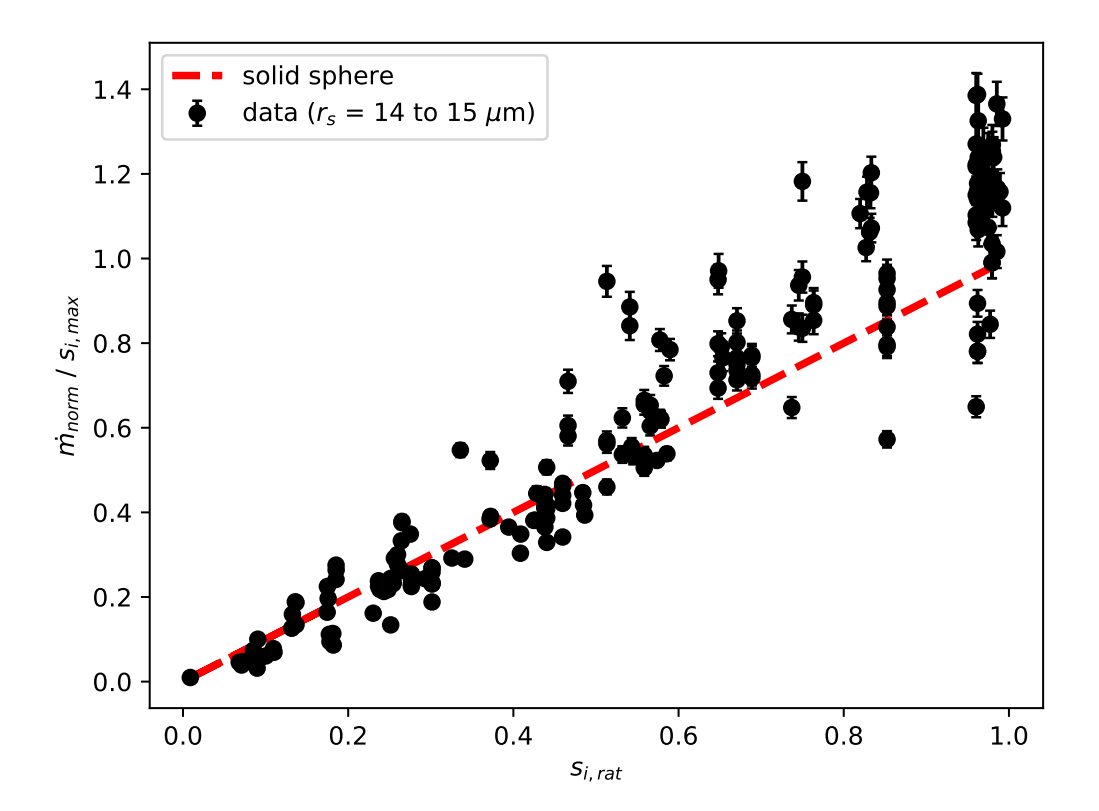


Fig. 3. Normalized growth rate divided by maximum supersaturation as a function of supersaturation ratio.

Black points are derived from data as the radius increases from 14 to 15 μ m, with error bars from uncertainty in

the initial size, temperature, and supersaturation. The red dashed line is from the capacitance growth rate of a

solid sphere.

likewise been scaled by $s_{i,max}$ to preserve the 1:1 relation for \dot{m}_{norm} of a solid sphere. The data 279 (black points) show that there are enhanced \dot{m}_{norm} values compared to a solid sphere, particularly 280 when $s_{i,rat} > 0.4$, and with increasing frequency and magnitude as liquid saturation is approached 281 (i.e. as $s_{i,rat} \rightarrow 1$). 282 Pokrifka et al. (2020) showed that some of their \dot{m}_{norm} values had a size dependence, indicating 287 that the growth could not be characterized by spheres growing at the capacitance rate. Many of the data here, especially at high $s_{i,rat}$, likewise have a size dependence. Figure 4 shows the mean 289 change in \dot{m}_{norm} for each particle as r_s increases from 9 to 25 μ m in 1- μ m increments ($d\dot{m}_{norm}/dr_s$). 290 For a solid sphere, this derivative is zero because \dot{m}_{norm} depends only on s_i . At low $s_{i,rat}$, there

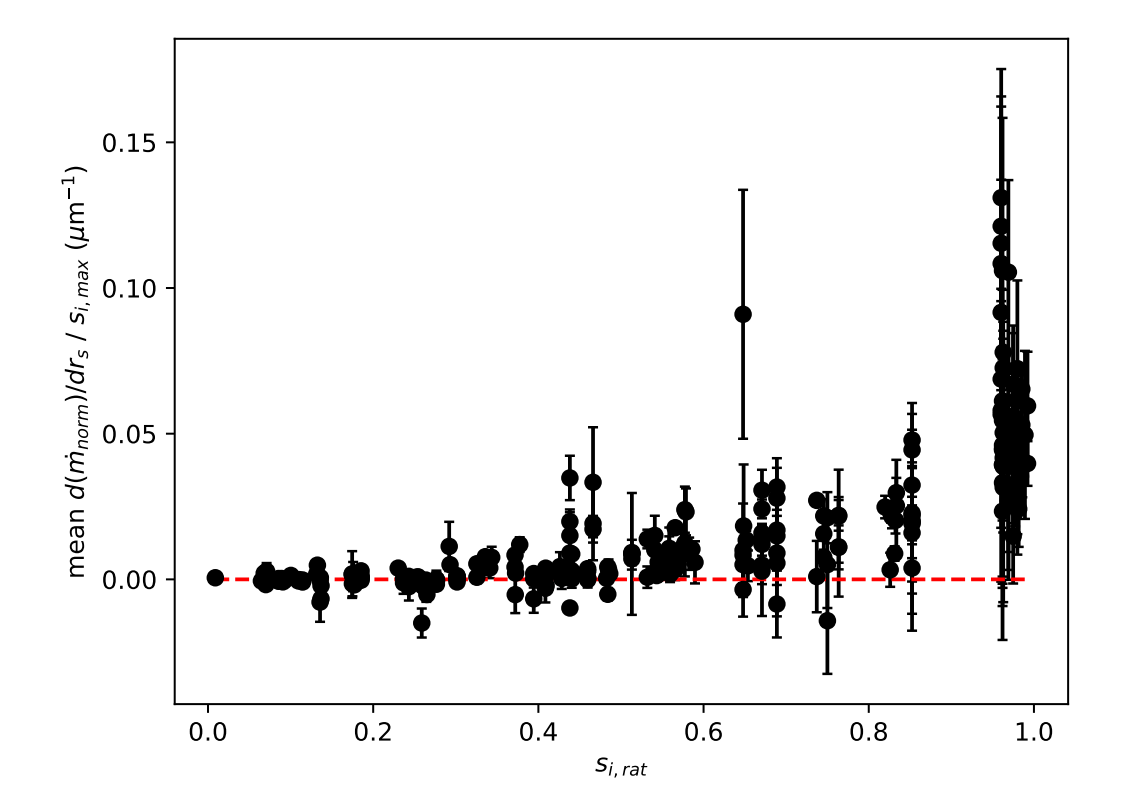


Fig. 4. Change in the normalized growth rate with respect to radius divided by the maximum supersaturation as a function of supersaturation ratio. Black points are mean values from the data, and the error bars indicate \pm one standard deviation. The red dashed line (zero) is for a solid sphere.

is indeed very little change to the normalized growth rate with size, indicating that these crystals grow near the spherical rate. However, at higher $s_{i,rat}$, most of the data have increasing normalized growth rates with increasing size. Similar to Fig. 3, the enhanced growth appears mostly when $s_{i,rat} > 0.4$, and it increases with supersaturation ratio, maximizing at liquid saturation. This result is consistent with what is expected if complex habits develop.

It is worth noting that some of the data initially have normalized growth rates less than a solid sphere, but the rates increase to exceed the solid sphere rate as the particles grow larger. This would make sense if the growth was limited by attachment kinetics, as for a faceted crystal, prior to the development of habit complexity. Before the facets formed, the mass growth rate would have been near that of a solid sphere (Nelson and Swanson 2019; Harrington and Pokrifka 2021). The

transition from frozen droplet to faceted crystal can cause a reduction in the deposition coefficient, though this transition sometimes happens too quickly to be detected in our experiments (Pokrifka et al. 2020). Harrington and Pokrifka (2021) showed that this transition is faster with increasing supersaturation, which means that we would most likely measure kinetics-limited growth rates at the beginning of high- s_i experiments.

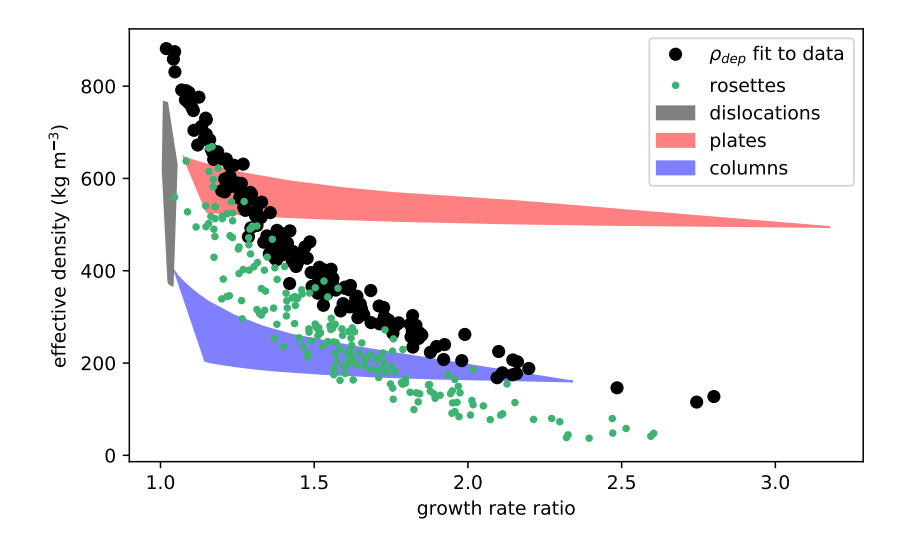
The above analyses of effective density fits to the mass ratio time-series and the normalized growth rate calculations make it clear that the growth enhancement at high supersaturation increases as a particle grows. Below, we investigate if the data can be represented by single- and polycrystalline ice growth models.

5. Time-Averaged Effective Density and Budding Rosette Model

The scatter in the growth data shown in Figs. 3 and 4 can be reduced if the data are examined as 315 a function of the amount of growth enhancement. For this, we define the growth rate ratio (\dot{m}_{rat}) 316 as the time-average measured growth rate divided by that of a solid sphere, where the averages 317 are taken over the lifetime of the particle. This ratio depends primarily on the crystal geometry, 318 because the supersaturation and temperature dependencies cancel. Note that there is a dependence 319 on attachment kinetics, but it is weak at high supersaturation. The top panel of Fig. 5 shows the time-average effective density for each particle from the fit with ρ_{dep} as a function of \dot{m}_{rat} (black 321 circles). The time-average effective densities derived from the power-law fitting method are similar 322 (not shown). Plotting against \dot{m}_{rat} clearly demonstrates that particles with more enhanced growth require smaller ρ_{eff} . The black circles in the lower panel of Fig. 5 show the exponents from the 324 power-law fitting method, also as a function of the growth rate ratio. Larger values of P correspond 325 to larger \dot{m}_{rat} , which is unsurprising since these results are a reflection of the effective density (Eq. 5). These results may seem intuitive, but what is most intriguing is how well the data points 327 organize when plotted against \dot{m}_{rat} for a relatively large temperature range (-65 to -40°C). Since 328 the growth rate ratio depends primarily on crystal geometry, the data organization indicates an 329 underlying similarity in the crystals grown in the diffusion chamber. This organization does not occur if the data are plotted against temperature or supersaturation (not shown). 331

To establish physical meaning in these results, and ensure that they are reasonable, it is prudent to compare them to modeled ice particle growth with known habits. We have already shown that

338



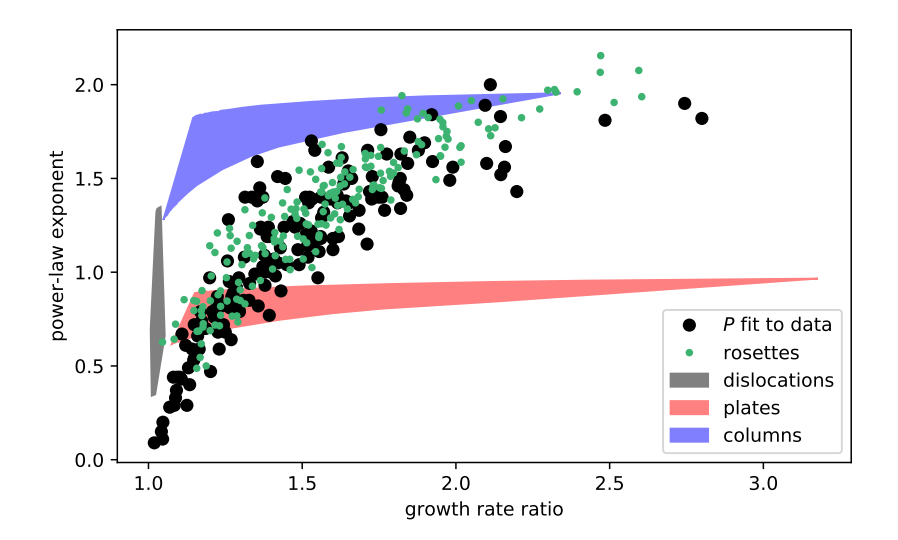


Fig. 5. Effective density (top) and power-law exponent (bottom) as a function of growth rate ratio. The black circles in the top panel are mean effective densities from fits to the mass ratio time-series using the deposition density. The black circles in the bottom panel are exponents from the best-fit to the data with the power-law method. In both panels, the shaded regions are from particles simulated by the DiSKICE model using dislocation growth for both plates and columns (grey) or ledge nucleation for plates (red) and columns (blue). The green points in both panels are from a budding rosette model.

a solid sphere underestimates the measured growth rates, however non-isometric shapes produce substantially enhanced growth (Takahashi et al. 1991). In the next section, we use the DiSKICE model to show that planar and columnar particles cannot explain the data, and that a budding rosette model can.

a. Effective density of single crystalline habits

We use DiSKICE to simulate the growth of single-crystalline particles, all of which are initially 345 spherical with a radius of 10 μ m. The crystals are grown for 15 minutes, which is typical for 346 our high- s_i growth experiments. To develop single-crystalline habit forms, a lesser characteristic 347 supersaturation (s_{char}) is required for the primary dimension of growth (i.e., the prism face for planar crystals, and the basal face for columnar crystals). Zhang and Harrington (2014) estimated 349 that s_{char} for the primary growing dimension is about 1/2 that of the minor dimension near -40°C, 350 and data at higher temperatures indicate that it is never less than 1/6. We use s_{char} values taken 351 from Harrington et al. (2019), however that work provides only the particle average value, therefore 352 we use the two ratios (1/2 and 1/6) as upper and lower estimates of s_{char} for the primary dimension. 353 In DiSKICE, the growth mechanism must also be specified. The freezing of supercooled water 354 produces numerous dislocations, and we therefore set M = 1 in Eq. 2 (see Harrington et al. 2019). This selection produces high deposition coefficients and is similar to the constant values used in 356 some cloud models. As crystals become larger, step nucleation can dominate the growth producing 357 thin plates or columns (Frank 1982; Nelson 2001), and we therefore also conduct simulations with M = 10. The temperatures are set at decades from -70 to -40°C, and supersaturation ratios ($s_{i,rat}$) 359 used are 0.25, 0.50, 0.75 and 1.00. 360

In Fig. 5, the range of the DiSKICE model solutions with dislocation growth is shown by the shaded grey region. All of these particles remain compact, as is to be expected for growth by dislocations (Harrington et al. 2019). The compact shape and high deposition coefficients prevent the growth rate ratio from becoming much greater than 1. The red and blue shaded regions of Fig. 5 correspond to the range of solutions for plates and columns, respectively, grown with step nucleation. Step nucleation produces thin plates and long columns, which succeeds in producing growth rate ratios greater than 2, as seen in the data, but there is very little overlap in the phase space. Note that the power-law exponent, *P*, approaches 1 for solid plates and 2 for solid columns

at the highest growth rate ratios, which is expected. For example, columns with the largest aspect ratios occur when growth on the prism faces is suppressed, producing growth that is essentially one-dimensional (along the c-dimension). Such crystals, therefore, should have a value of P that approaches 2. The data suggest that some of the particles grown in the diffusion chamber were columnar, but it is unlikely that we grew dislocation-dominated crystals or single-crystalline plates.

b. Budding rosette growth model

Since polycrystals, especially rosette crystals, nucleate often at temperatures less than -40°C (Heymsfield et al. 2002; Bacon et al. 2003; Bailey and Hallett 2009; Lawson et al. 2019), we also compare our results to a model of budding rosette growth. Our model is similar to that of Um and McFarquhar (2011), except we combine the rosette capacitance models of Westbrook et al. (2008) and Chiruta and Wang (2003) with a central sphere. We then obtain instantaneous growth rates for known particle shapes from which effective densities can be calculated.

We begin with an ice sphere with an initial radius r_0 , like our experiments. As the particle grows, n_b number of bullets protrude out of the sphere (see Fig. 6). Measurements of frozen drops indicate that this begins with the development of small facets on the surface that can grow outwards becoming the branches of a budding rosette (Parungo and Weickmann 1973, conceptual sequence in their Fig. 10). Each bullet is comprised of a hexagonal column 2c in length and 2a in width, which has a volume

$$V_{col} = 3\sqrt{3}a^2c,\tag{9}$$

with the addition of a pyramidal region connecting it to the sphere. We follow Westbrook et al. (2008) and define the volume of the hexagonal pyramid as $V_{hexp} = f_{pyr}\sqrt{3}a^2c$, where the height of the pyramid (h_p) is defined as a fraction f_{pyr} of the column length such that $h_p = 2cf_{pyr}$. We subtract off the volume of the pyramidal peak V_{peak} to allow for some contact area with the sphere. The contact region is $2a_0$ across, where a_0 is a fraction f_{a0} of the radius of the sphere r_0 (i.e., $a_0 = f_{a0}r_0$). The height of the removed peak is therefore $h_0 = h_p a_0/a$, and the volume of the removed peak is $V_{peak} = (\sqrt{3}/2)a_0^2h_0$. The total volume of the pyramidal region becomes

$$V_{pyr} = V_{hexp} - V_{peak} = f_{pyr} \sqrt{3}a^2 c \left[1 - \left(\frac{a_0}{a} \right)^3 \right].$$
 (10)

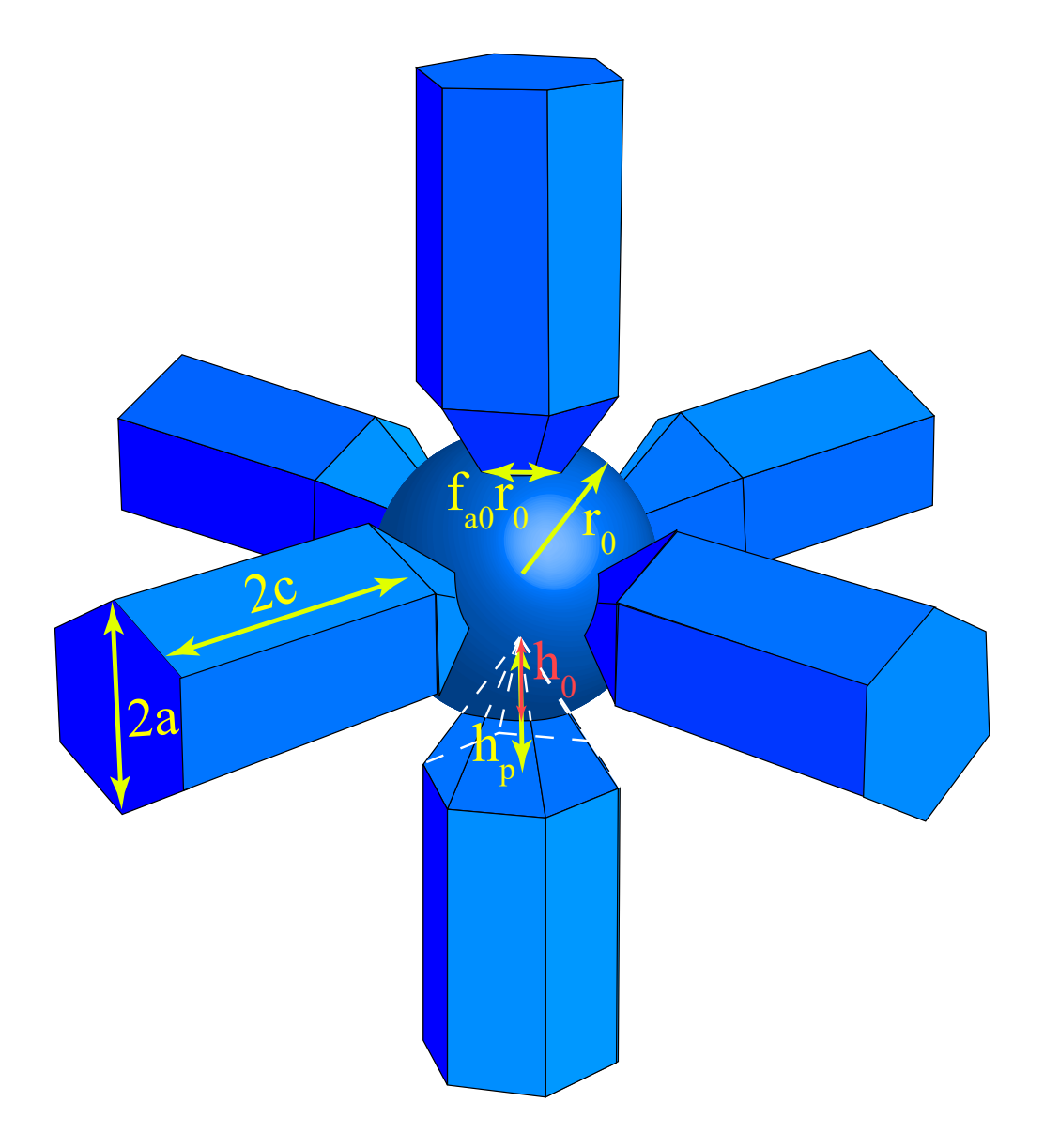


Fig. 6. Schematic of the budding rosette model. Each bullet has a length 2c, a width 2a, and a pyramidal "tip" that intersects with the central sphere, which itself has a radius r_0 . Each pyramid has a total height h_p , with a portion h_0 long removed from the peak such that intersection with the sphere is $f_{a0}r_0$ across.

Thus, the budding rosette volume is

$$V_{ros} = \frac{4}{3}\pi r_0^3 + n_b(V_{col} + V_{pyr}), \tag{11}$$

with effective density

$$\rho_{eff} = \frac{\rho_i V_{ros}}{\frac{4}{3} \pi r_{eff}^3}, \text{ where } r_{eff} = r_0 + 2c \left(1 + f_{pyr} \frac{a}{a_0} \right), \tag{12}$$

assuming a symmetrical rosette.

To compare this model to our data, the growth rate for a budding rosette is needed, and this requires the capacitance. The capacitance of a rosette depends on the maximum dimension and the aspect ratio ($\phi = c/a$) of the branches. The branch aspect ratio is determined using the ratio of the a- and c-dimension deposition coefficients following Nelson and Baker (1996),

$$\frac{dc}{da} = \frac{\alpha_c}{\alpha_a} \equiv \Gamma. \tag{13}$$

We calculate the capacitance of a bullet rosette with n_b branches of aspect ratio ϕ as

$$C = 0.35\phi^{-0.27}D_{max}$$
 if $n_b = 4$ (Westbrook et al. 2008, their Eq. 5)
 $C = 0.40\phi^{-0.25}D_{max}$ if $n_b = 6$ (Westbrook et al. 2008, their Eq. 6)
 $C = 0.40\left(\frac{n_b}{6}\right)^{0.257}\phi^{-0.25}D_{max}$ if $n_b > 6$ (Chiruta and Wang 2003, based on their Eq. 15), (14)

where $D_{max} = 4c(1 + f_{pyr})$ is the maximum dimension of a rosette with four or six branches (Westbrook et al. 2008). To approximate the capacitance for rosettes with more branches, we use the capacitance from Chiruta and Wang (2003). Their parameterization is valid for rosettes with 2 to 16 branches, but it is independent of the branch aspect ratio. We therefore estimate the ϕ -dependence using the six-branch capacitance of Westbrook et al. (2008), ensuring that the equations match for $n_b = 6$. Since the exponent on ϕ appears to be weakly dependent on n_b (see the first two equations in Eq. 14), this approximation is justifiable.

The growth of a budding rosette requires the inclusion of the spherical core, an influence that needs to be estimated. Growth from vapor deposition depends on the surface area multiplied by the vapor diffusion flux. For a sphere this goes as $4\pi r_0^2 \times (D_{eff} s_i \rho_{eq}/r_0)$. For a non-spherical crystal, Nelson (1994, pg 52, Eq. 3.1) suggests C is the appropriate length scale for the flux, the growth rate then goes as $4\pi C^2 \times (D_{eff} s_i \rho_{eq}/C)$. As an approximation, we follow Harrington and Pokrifka (2021) and write the growth of a budding rosette as a weighted combination of these

fluxes, using the weighting factor

$$w = \frac{A_{int}}{A_{scl}} = \frac{4\pi r_0^2}{4\pi (r_0^2 + C^2)},\tag{15}$$

where A_{int} is the surface area of the sphere and A_{scl} is a "scaling" surface area of the sphere and the branches. This latter area is, in a sense, a total area for vapor diffusion. The growth rate of a budding rosette is therefore approximately

$$\frac{dm}{dt}_{ros} \simeq A_{scl} \left(w \frac{D_{eff} s_i \rho_{eq}}{r_0} + (1 - w) \frac{D_{eff} s_i \rho_{eq}}{C} \right) = 4\pi (r_0 + C) D_{eff} s_i \rho_{eq}, \tag{16}$$

where the right-most form results from substitution of the total area and the weight. Note that the growth length scale simply becomes the initial radius plus the capacitance of the branches. Since the crystals begin without branches, this equation reduces to that of a sphere, as expected. To compare directly to the data requires the growth rate ratio averaged over the growth time-series which is

$$\dot{m}_{rat} = \overline{\left(\frac{r_0 + C}{r_s}\right)}. (17)$$

where r_s is the solid-sphere radius.

The evolution of a budding rosette is simulated using the geometry (Eqs. 11 and 12) with the 428 growth equation (Eq. 16). Our measurements provide the ranges for the initial radius (5 - 20 μ m) 429 and the final mass ratio (8 - 18), but f_{pyr} , f_{a0} , Γ , n_b , must be prescribed in this model. These values are given reasonable ranges based on geometry and prior measurements. For example, Γ 431 may be unity, producing compact branches, or it may be as large as 20 (Harrington et al. 2019, 432 their Fig. 12) causing the branches to become long and thin. We set n_b to 4, 6, or 10, based on 433 observations that rosettes can have at least 8 branches (Heymsfield and Iaquinta 2000) and prior 434 theoretical calculations providing the capacitance for 4, 6 (Westbrook et al. 2008) and up to 16 435 branch rosettes (Chiruta and Wang 2003). If n_b is 4 or 6, we set f_{a0} to be within the range of 0.5 436 - 0.9. Since f_{a0} controls that amount of the internal sphere's surface area that is covered by each branch, it is reduced to be 0.2 - 0.5 when $n_b = 10$ to accommodate the larger number of branches. 438 These ranges are based on estimates of the number of hexagonal facets that can reasonably tile 439

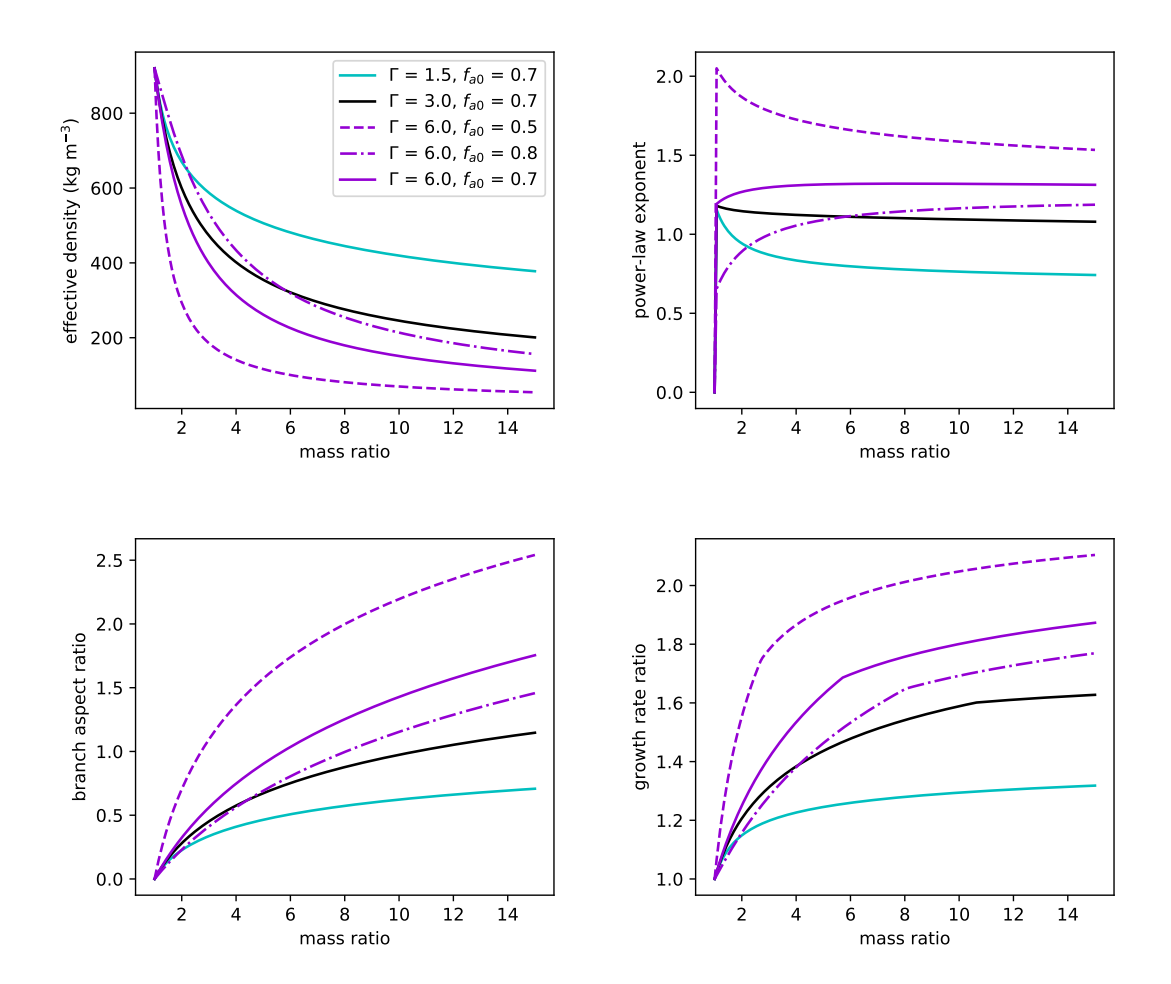


Fig. 7. Example budding rosette simulations with six branches and an initial radius of 10 μ m. Cyan, black, 442 and purple curves have Γ set to 1.5, 3.0, and 6.0, respectively. Dashed, solid, and dot-dashed curves have f_{a0} set 443 to 0.5, 0.7, and 0.8, respectively. Plotted is the effective density (upper left), power-law exponent (upper right), 444 branch aspect ratio (lower left), and growth rate ratio (lower right) as a function of mass ratio. 445

the surface of a sphere, following the model of Harrington and Pokrifka (2021). Westbrook et al. (2008) assumes a value of 0.5 for f_{pyr} , which we expand to a range of 0.2 - 0.6. 441 Figure 7 shows the simulated growth of selected, six-branched particles following Eqs. 9 - 17, all 446 of which use $r_0 = 10 \mu \text{m}$, final $m_r = 15$ and $f_{pyr} = 0.5$. Unsurprisingly, increasing Γ (cyan to black to purple solid curves) causes a larger decrease in the effective density and increase in the power-448

440

law exponent. That is, increasing the growth of the c-dimension with respect to the a-dimension 449 causes the branches to become thinner (larger aspect ratio), lowering the effective density. The

resulting branch aspect ratios are quite reasonable, reaching 1.5 - 2.5 when Γ = 6. Decreasing f_{a0} (dot-dashed to solid to dashed purple curves) produces thinner branches, a decreased effective density and an increased power-law exponent. This also makes physical sense, because a smaller initial branch area spaces them further apart and makes them thinner. Furthermore, both increasing Γ and decreasing Γ and decreasing Γ produce enhanced growth rates, with growth rate ratios ranging from 1 to Γ these values of effective density, power-law exponent, and growth rate ratio are in good agreement with the data (Fig. 5).

The results from Fig. 7 clearly indicate that growth rate ratio and effective density depend on the 458 manner in which branches form (through surface area coverage) and the resulting aspect ratios of 459 the branches (controlled by the deposition coefficient ratio Γ). The variability in the data shown 460 in Fig. 5 (black circles) is therefore not surprising. To emulate the data, we ran many additional 461 simulations with the budding rosette model (Eqs. 9 - 17), the results of which are shown as green 462 points in Fig. 5. Each point is from one growth simulation, and the variability is from random 463 selections of r_0 , f_{pyr} , f_{a0} , n_b , Γ and the final mass ratio using the ranges discussed above. These results strongly resemble the data and imply that the particles grown in the laboratory were likely 465 polycrystalline, and may well have been budding rosettes. Simulations with a polycrystalline plate 466 model does not produce a match with the data, since the points scatter near P = 1 (not shown), which is reasonable for planar particles. 468

The match of the budding rosette model with the data also provides indirect corroboration of the classical geometric rosette model for cloud modeling applications. However, using this model requires a number of unknown parameters, including the number of branches and branch aspect ratio, which makes fitting the growth data with the budding rosette model unjustified. The measured mass ratio time-series and initial size are not enough to adequately constrain the unknown parameters. Thus, the parameterizations that we develop in the following section are derived entirely from the laboratory data, independent of the budding rosette model. The advantage in using the simplified effective density in a parameterization is that the unknown parameters are implicitly included.

6. Supersaturation dependence and parameterization of the effective density

The strong correlation between the effective density and the growth rate enhancement indicates 479 that there is structural regularity to the measured data that should also appear as a function of the supersaturation, even though such regularity is not apparent in Figs. 3 and 4. For completeness, we 481 include the data at low supersaturation, which often show evidence of attachment kinetic limitations 482 (Pokrifka et al. 2020). To further investigate the supersaturation dependence to growth, we examine the fraction of experiments with kinetic limitations (growth rate ratio; 1) as compared to those 484 with enhanced growth (growth rate ratio i, 1). If we calculate this fraction in supersaturation ratio 485 bins of 0.0 - 0.4, 0.4 - 0.6, 0.6 - 0.8, and 0.8 - 1.0 (Fig. 8), it becomes clear that kinetics-limited growth (dashed) is more common when the $s_{i,rat}$ is lower, whereas enhanced growth is common 487 when $s_{i,rat}$ is high (solid). The increased occurrence of enhanced growth with increasing $s_{i,rat}$ 488 reflects the results shown in Fig. 4. Note that a similar result appears when $s_{i,rat}$ ranges of 0 - 0.2 489 and 0.2 - 0.4 are used, as little growth enhancement occurred at $s_{i,rat} < 0.4$ (Fig. 4), thus we use the combined range of 0 - 0.4 for clarity, and do so for the remainder of this work. This $s_{i,rat}$ range 491 is well represented by solid ice, however attachment kinetics must be included to properly account 492 for the mass growth rate (Pokrifka et al. 2020).

We should expect an approximately monotonic rise in the relative frequency of enhanced growth cases with supersaturation ratio, but variability within a given $s_{i,rat}$ range is also to be expected, since crystals nucleated from frozen water droplets will vary in their morphological complexity (Bacon et al. 2003). Such variability is shown in Fig. 9 through a 2-dimensional (2-D) distribution of the relative frequency of cases as a function of the supersaturation ratio and the growth rate ratio for the entire dataset. This 2-D distribution confirms that increasing $s_{i,rat}$ increases the likelihood of particles growing at enhanced rates and that low $s_{i,rat}$ often produces kinetics-limited growth that can be approximated as solid ice (i.e., $\rho_{dep} = 920 \text{ kg m}^{-3}$ and P = 0).

It is important to note that while the 268 experiments we conducted are numerous for individual crystal studies, the data are too few for a detailed statistical analysis. In addition, there are relatively fewer data at $s_{i,rat} \leq 0.2$. Experiments at $s_{i,rat} \leq 0.2$ are challenging, since they take a whole day to conduct due to very small particle growth rates. This is in contrast to higher- $s_{i,rat}$ experiments, where multiple particles can be grown within a day. However, most of the high- $s_{i,rat}$ (≥ 0.8) experiments were conducted around the low-to-mid portion of the temperature

507

509

510

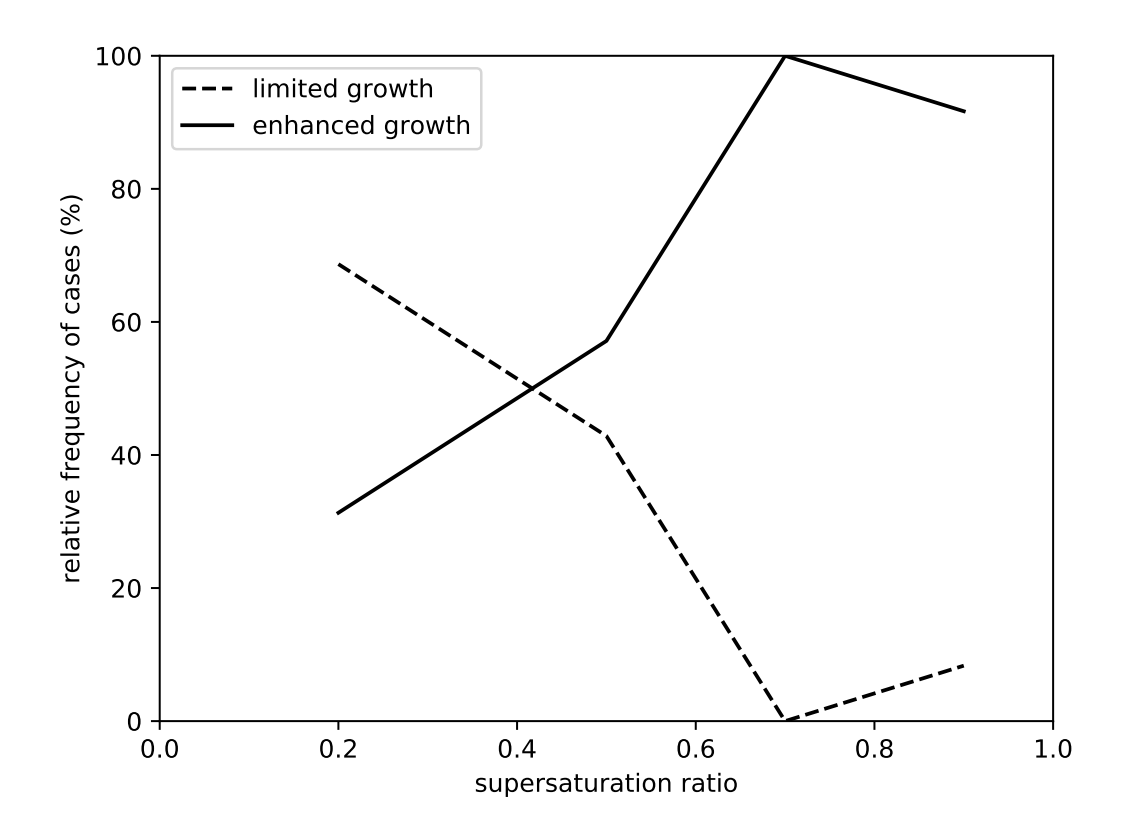


Fig. 8. Fraction of particles in the dataset that show enhanced growth (solid) or limited growth (dashed) in supersaturation ratio bins of 0.0 - 0.4, 0.4 - 0.6, 0.6 - 0.8, and 0.8 - 1.0.

range (i.e., -63 to -53°C). To examine the potential impact of this sample bias, we split the dataset into "warm" (T > -56°C) and "cold" (T < -56°C) subsets. We indeed find that "warm" cases more frequently occur at low- $s_{i,rat}$ and low- \dot{m}_{rat} , and vise versa for "cold" cases, but both subsets demonstrate increasing \dot{m}_{rat} with increasing $s_{i,rat}$ (not shown). Thus, the precise value and location of the maximum in Fig. 9 may change with more even sampling, but the positive correlation of supersaturation ratio and growth rate ratio is robust for both data subsets. This result indicates that $s_{i,rat}$ is an environmental condition that may be utilized in conjunction with our data to produce parameterizations of effective density. We will also demonstrate that the sample bias has minimal effect on these parameterizations.

Given the systematic correlation of the growth rate ratio with the supersaturation ratio, we should expect the effective density to behave in a similar fashion. Figure 10 shows the relative frequency

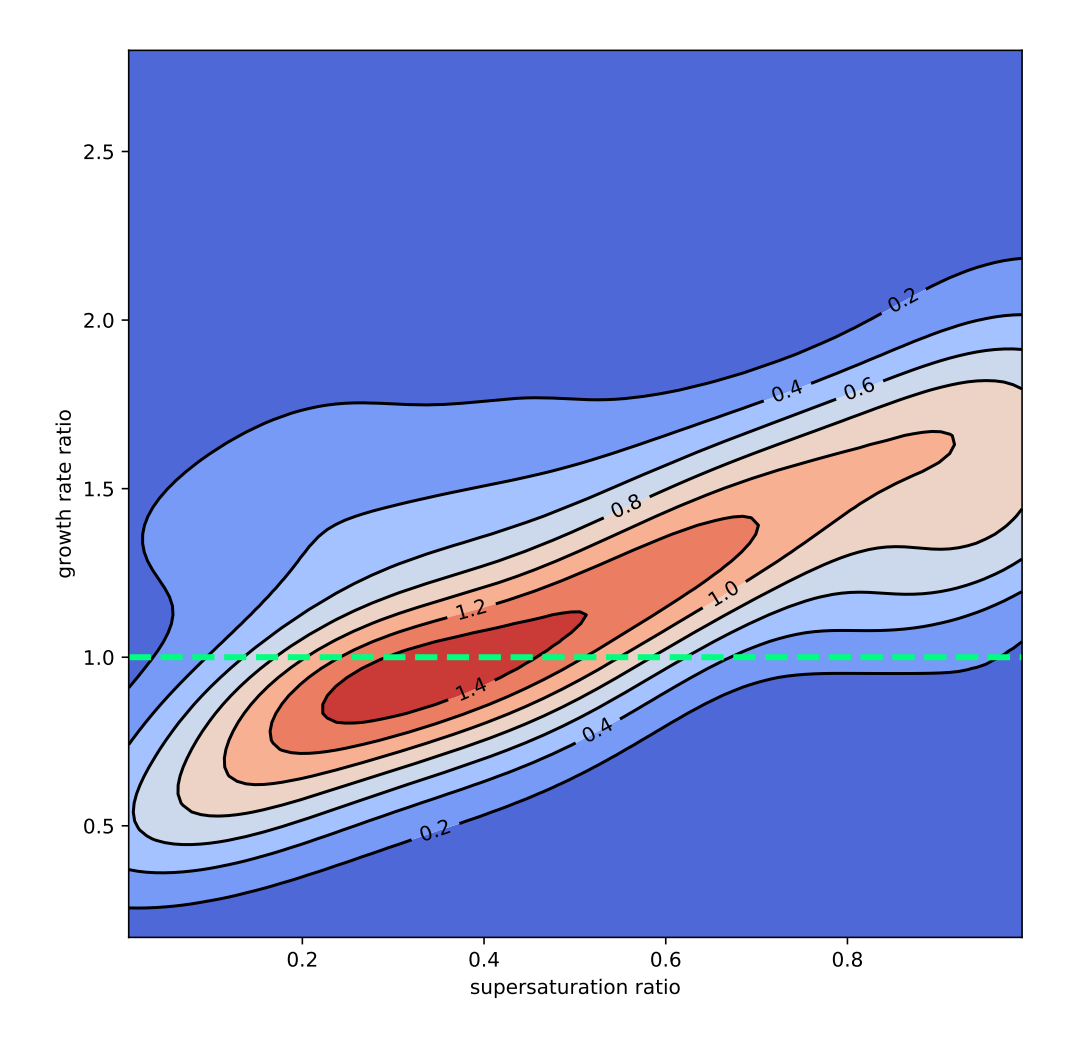


Fig. 9. Two-dimensional relative frequency distribution of supersaturation ratio versus growth rate ratio.

Increasingly red contours indicate increasing occurrence. The green dashed line is where the growth rate ratio is

unity, as for a solid sphere: Above this line growth is enhanced, below it growth is limited.

of ρ_{dep} values derived from the fits (Eqs. 3 and 4) for all of the experiments in supersaturation ratio bins of 0 - 0.4 (cyan), 0.4 - 0.6 (blue), 0.6 - 0.8 (purple), 0.8 - 1 (black). To demonstrate the overall trend in each $s_{i,rat}$ bin, the ρ_{dep} values are separated in bins of 0 - 300, 300 - 600, $600 - 920 \text{ kg m}^{-3}$. The relative frequencies are also listed in Table 2. It is clear from Fig. 10 that conditions with $s_{i,rat} < 0.6$ often produce high values of ρ_{dep} , and small ρ_{dep} values are rare.

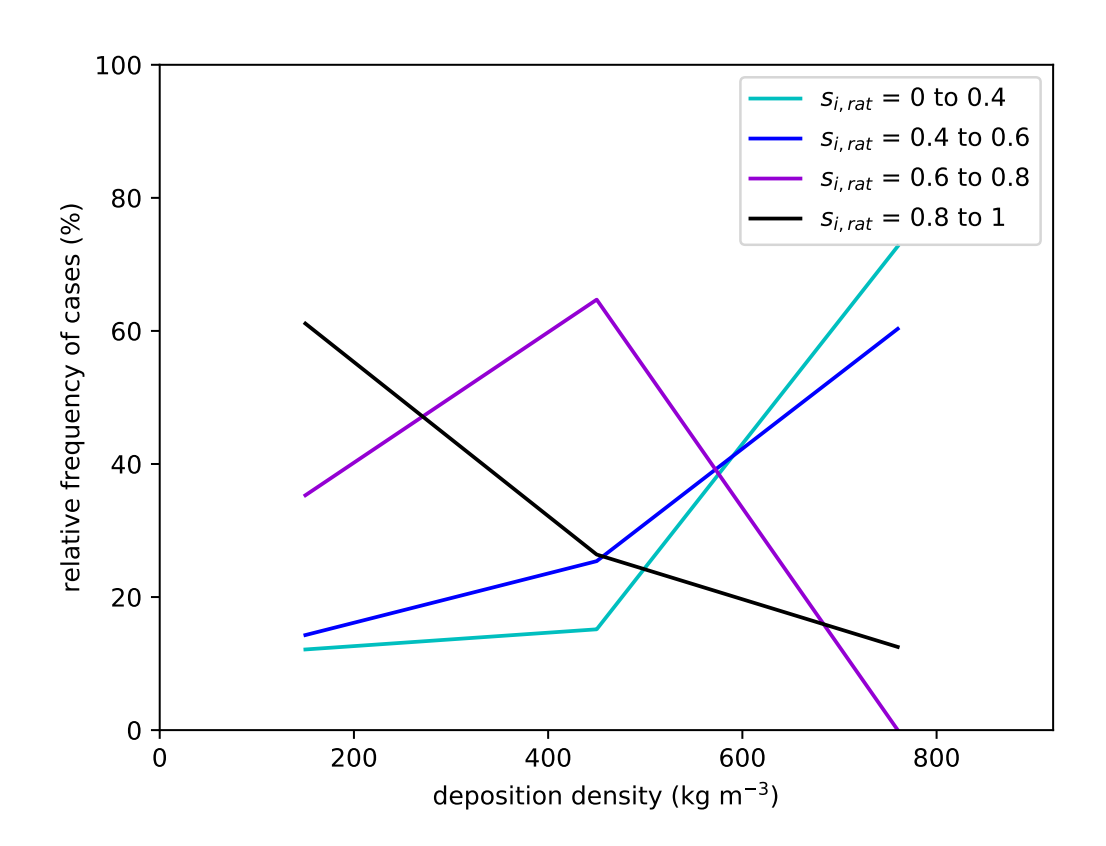


Fig. 10. Relative frequency of cases producing deposition densities in ranges of 0 - 300, 300 - 600, and $600 - 920 \text{ kg m}^{-3}$, in supersaturation ratio bins of 0.0 - 0.4 (cyan), 0.4 - 0.6 (blue), 0.6 - 0.8 (purple), and 0.8 - 1.0 (black).

As $s_{i,rat}$ increases, so does the frequency of smaller ρ_{dep} values, such that $\rho_{dep} > 600 \text{ kg m}^{-3}$ is the rarity when $s_{i,rat} > 0.6$. Unsurprisingly, supersaturation near liquid saturation ($s_{i,rat} = 0.8$) most frequently produces the smallest values of ρ_{dep} , which are associated with the greatest degree of growth enhancement. The supersaturation ratio dependence of the time-averaged effective density (Fig. 11, solid curves) is similar to that of ρ_{dep} , though the values of ρ_{eff} are larger. This is expected because ρ_{eff} approaches ρ_{dep} as crystal size increases.

A 2-D relative frequency distribution of the deposition density and supersaturation ratio (Fig. 12) provides a more succinct visualization of the information in Fig. 10. The distribution highlights two local maxima of the relative frequency. One maximum appears for values of $s_{i,rat} < 0.4$, and it corresponds to particles with high density ($\rho_{dep} \sim \rho_i$). As the supersaturation ratio approaches

546

547

Table 2. Relative frequencies of deposition density, effective density from ρ_{dep} —fits, and power-law exponent for experiments in supersaturation ratio bins of 0 - 0.4, 0.4 - 0.6, 0.6 - 0.8, and 0.8 - 1. The densities are in ranges of 0 - 300, 300 - 600, and 600 - 920 kg m⁻³, and the power-law exponents are in ranges of 0 - 0.5, 0.5 - 1, 1 - 1.5, and 1.5 - 2.

supersaturation ratio	deposition density (kg m ⁻³)			effective	effective density (kg m ⁻³)		power-la	power-law exponent			
	0 - 300	300 - 600	600 - 920	0 - 300	300 - 600	600 - 920	0 - 0.5	0.5 - 1	1 - 1.5	1.5 - 2	
0 - 0.4	12.1%	15.2%	72.7%	5.0%	19.2%	75.8%	71.7%	12.1%	10.1%	6.1%	
0.4 - 0.6	14.3%	25.4%	60.3%	9.5%	25.4%	65.1%	61.9%	15.9%	17.4%	4.8%	
0.6 - 0.8	35.3%	64.7%	0.0%	8.8%	82.4%	8.8%	0.0%	41.2%	50.0%	8.8%	
0.8 - 1	61.1%	26.4%	12.5%	32.0%	48.6%	19.4%	9.7%	11.1%	48.6%	30.6%	

liquid saturation, ρ_{dep} falls and there is another maximum at $\rho_{dep} \sim 250 \text{ kg m}^{-3}$. To estimate the most likely values of ρ_{dep} at some $s_{i,rat}$, we fit a linear function between both maxima (dark green dashed line). At low $s_{i,rat}$, we find the linear fit from $s_{i,rat} = 0$ and $\rho_{dep} = 920 \text{ kg m}^{-3}$ to the high-density local maximum (light green dashed line). The two linear fits cover all values of $s_{i,rat}$ from our experiments and are given by

$$\rho_{dep}(s_{i,rat}) = \begin{cases} -32.332s_{i,rat} + 920, & s_{i,rat} \le 0.267\\ -1027.456s_{i,rat} + 1185.834, & s_{i,rat} > 0.267 \end{cases} ,$$
 (18)

where the coefficients have units of kg m⁻³. A mass-size relationship can then be derived by substituting Eq. 18 into Eq. 4,

$$m(\rho_{dep}) = \frac{4}{3}\pi \rho_{eff}(\rho_{dep})r^3 = \frac{4}{3}\pi \{ [\rho_i - \rho_{dep}(s_{i,rat})]r_0^3 + \rho_{dep}(s_{i,rat})r^3 \}.$$
 (19)

Here, r is the the radius of the sphere encompassing the particle, or the maximum semi-dimension. Equations 18 and 19 comprise a parameterization of the effective density as a function of ρ_{dep} at low temperatures suitable for particle property microphysical models rooted in the method of Chen and Lamb (1994), such as Hashino and Tripoli (2007), Chen and Tsai (2016), and Jensen et al. (2017). Those models currently use $\rho_{dep} \simeq \rho_i$ at temperatures below -20°C. Note that Eq. 19 is strictly valid for constant $s_{i,rat}$. We discuss below how to utilize this parameterization with variable temperature and supersaturation.

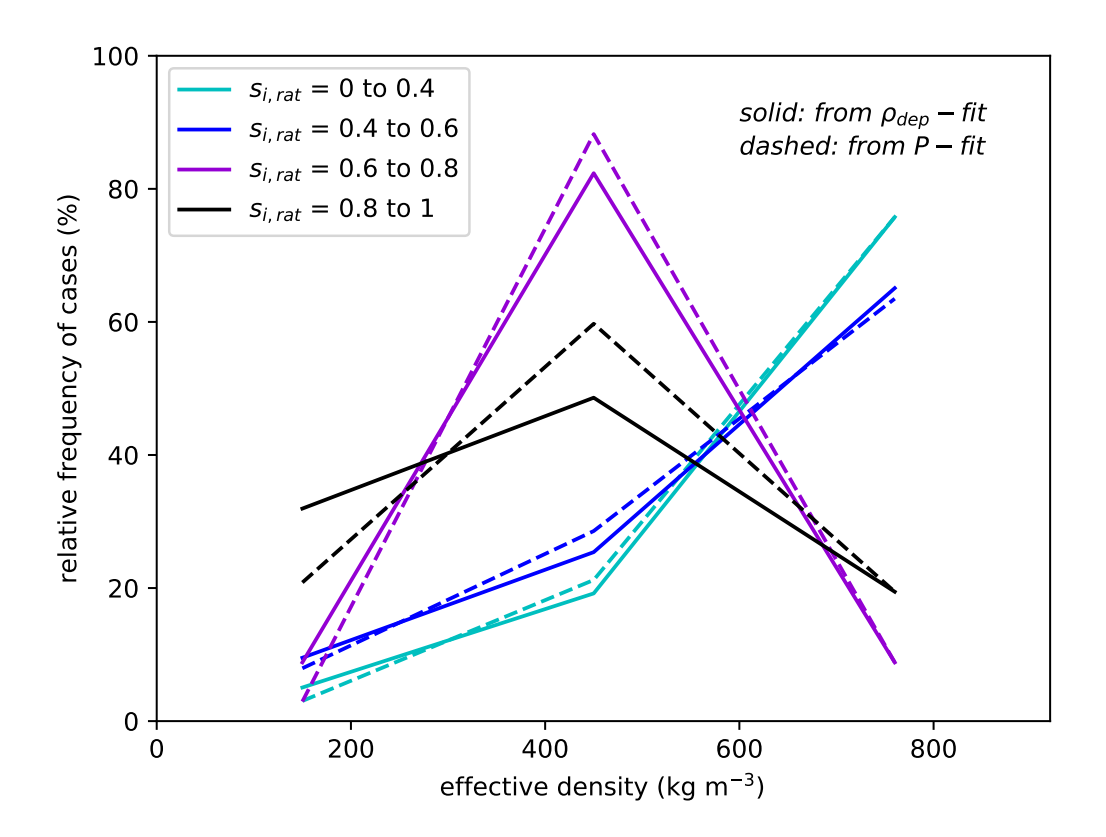


Fig. 11. Relative frequency of cases producing mean effective densities in ranges of 0 - 300, 300 - 600, and 600 - 920 kg m⁻³, derived from the deposition density (solid) and power-law (dashed) for the same supersaturation ratio bins as in Fig. 10.

To test the potential impact that a sampling bias may have on this parameterization, we repeat the above linear fitting procedure with data in the range $0.2 < s_{i,rat} < 0.8$ (purple dot-dashed curve in Fig. 12). This range of supersaturation ratio eliminates the regions where most of the sampling bias occurred. Using only data where $0.2 < s_{i,rat} < 0.8$ produces the same trend as the whole dataset, but with a slightly larger slope (compared to the green dashed curve). This change in slope makes sense in comparison to Fig. 10, which shows that disregarding $s_{i,rat} > 0.8$ would shift the most frequent values of ρ_{dep} at high $s_{i,rat}$ to be 300 - 600 kg m⁻³. Because the data between $0.2 < s_{i,rat} < 0.8$ are evenly sampled, we can also test for a temperature-dependence in our parameterization method. While using the supersaturation ratio provides a common, temperature-independent scale to analyze the data, temperature has other influences, such as in crystal morphology and attachment kinetics.

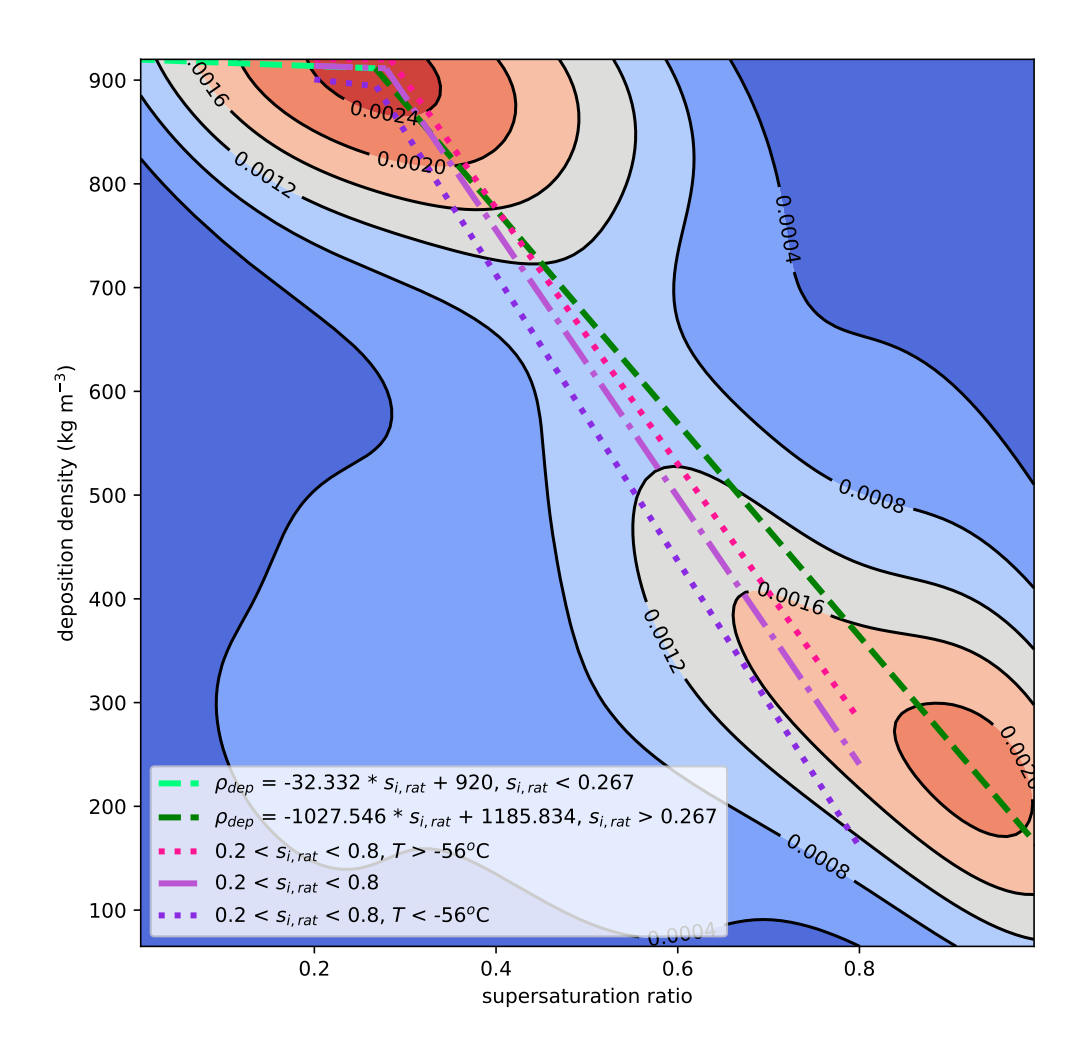


Fig. 12. Two-dimensional relative frequency distribution of supersaturation ratio versus deposition density. Increasingly red contours indicates increasing number of occurrences. The light green dashed curve is a linear fit from the $(s_{i,rat} = 0, \rho_{dep} = 920 \text{ kg m}^{-3})$ coordinate to the nearest local maximum, and the dark green dashed curve is a linear fit between the two maxima. The purple dash-dotted curve is the same as the green dashed curves, but using only cases with $s_{i,rat}$ between 0.2 and 0.8. The pink and indigo dotted curves are the same as the purple dash-dotted curve, but with the temperatures restricted to above -56°C and below -56°C, respectively.

As before, we have split the dataset into cold and warm regions at -56°C, and the resulting curves are plotted on Fig. 12. For T > -56°C (pink dotted curve) the slope decreases, and for T < -56°C

(indigo dotted curve) the slope increases. This small variation indicates that the temperature dependence of ρ_{dep} is second-order compared to the primary dependence on $s_{i,rat}$, which seems well characterized by our data.

Traditional microphysical schemes parameterize the effective density and the mass with power laws, and we therefore follow the above method to estimate the most likely value for the power-law 585 exponent P for Eqs. 5 and 6. Figure 13 shows the relative frequency of observed P values for 586 the same supersaturation ratio ranges used in Fig. 10 (see also Table 2). Here, the power-law 587 exponents are binned into ranges of 0 - 0.5, 0.5 - 1, 1 - 1.5, and 1.5 - 2. Similar to Fig. 10, 588 lower supersaturation ratios $s_{i,rat} < 0.6$ (cyan and blue curves) produce little enhanced growth and, 589 therefore, values of $P \sim 0$ occur frequently. Increasing $s_{i,rat}$ (to purple then black curves) increases 590 the frequency of P values associated with greater growth enhancement. Again, the largest amount 591 of growth enhancement is most common near liquid saturation (black curve), but even under these 592 conditions, P is most frequently in the range of 1 - 1.5 instead of 1.5 - 2. Since $P \sim 2$ is consistent 593 with columnar growth (note that hollow columns can have P > 2), it is interesting that the fraction of particles grown near liquid saturation with $P \sim 2$ (30.6%) is close to the fraction of columns that 595 Bailey and Hallett (2004) grew under similar conditions (Hashino and Tripoli 2008, see their Fig. 596 1). Additionally, the power-law produces time-averaged ρ_{eff} relative frequencies that are similar to those calculated from ρ_{dep} , but with values of 300 - 600 kg m⁻³ being slightly more common 598 (Fig. 11, dashed curves). 599

Like ρ_{dep} , the variability in P with supersaturation ratio can be better visualized with a 2-D distribution. Figure 14 shows two local maxima corresponding to those of Fig. 12. One maximum is at low $s_{i,rat}$ associated with high density particles ($P \sim 0$) and growth limited by attachment kinetics. The second maximum occurs at high $s_{i,rat}$ where growth is enhanced ($P \sim 1.4$). To estimate a most likely value of P at high $s_{i,rat}$ we fit a line through both maxima (dark green dashed line). The value of P is estimated at low- $s_{i,rat}$ values with a linear fit from $s_{i,rat} = 0$ and P = 0 to the nearest local maximum (light green dashed line). The most likely value of P for each $s_{i,rat}$ is thus estimated to be

$$P(s_{i,rat}) = \begin{cases} 0.082s_{i,rat}, & s_{i,rat} \le 0.267\\ 2.106s_{i,rat} - 0.541, & s_{i,rat} > 0.267 \end{cases}$$
 (20)

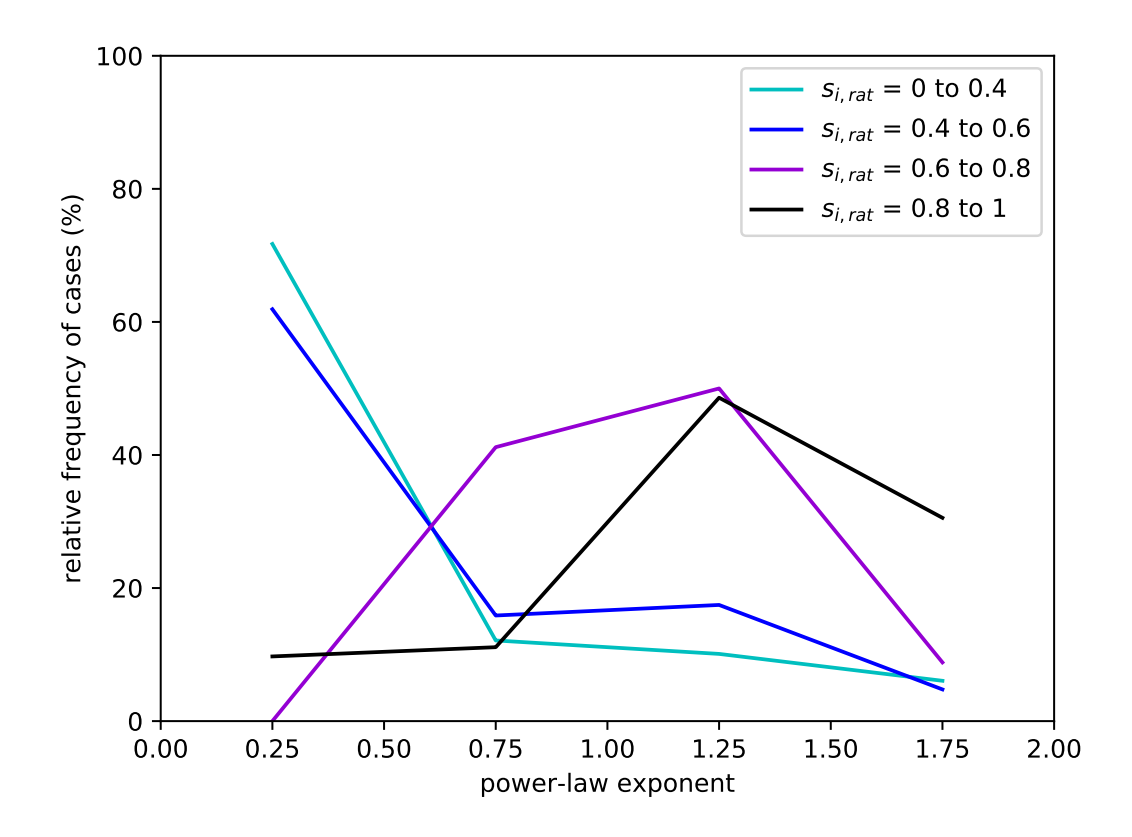


Fig. 13. Relative frequency of cases producing power-law exponents in ranges of 0 - 0.5, 0.5 - 1, 1 - 1.5, and
1.5 - 2 for the same supersaturation ratio bins as in Fig. 10

Combining Eq. 20 with Eq. 5 provides a parameterization for the effective density of small vapor grown crystals. This parameterization therefore produces a supersaturation-dependent power-law,

$$m(P) = \frac{4}{3}\pi \rho_{eff}(P)r^3 = \frac{4}{3}\pi \rho_i r_0^{P(s_{i,rat})} r^{3-P(s_{i,rat})}.$$
 (21)

It should be noted that the sampling bias and temperature dependence shown for Fig. 12 is less pronounced for the distribution of P, and is therefore not shown. Because Eqs. 18 - 21 were derived from the measured growth of small particles ($r \sim 10 - 100 \mu m$) at temperatures between -65 and -40°C, these parameterizations may not be applicable to other conditions. Like Eq. 19, Eq. 21 is strictly valid for constant $s_{i,rat}$ (i.e., constant temperature and supersaturation). When the supersaturation ratio is variable, as in a real cloud, care must be taken in using Eq. 21. Since the power-law exponent changes with supersaturation ratio, one cannot simply change P in Eq. 21, as

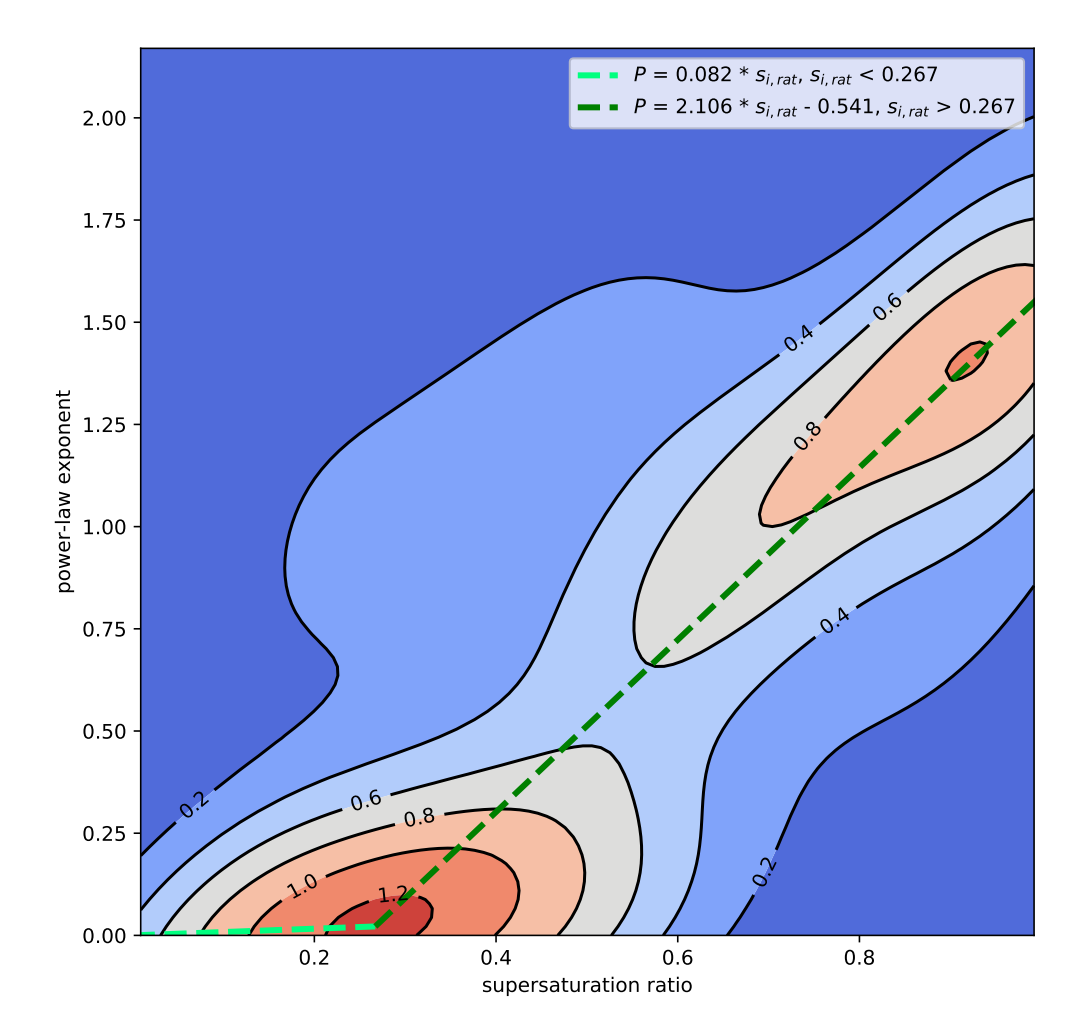


Fig. 14. Two-dimensional relative frequency distribution of supersaturation ratio versus power-law exponent.

Increasingly red contours indicates increasing number of occurrences. The light green dashed curve is a linear fit from the $(s_{i,rat} = 0, P = 0)$ coordinate to the nearest local maximum, and the dark green dashed curve is a linear fit between the two maxima.

this would instantaneously change the particle characteristics. Instead, the approach we advocate is to calculate the deposition density by taking the time-derivative of either Eq. 19 or 21 (depending on the chosen parameterization), which will result in either Eq. 3 or 6, respectively. The particle effective density is then updated using Eq. 4. The physical interpretation is that the change in $s_{i,rat}$ influences the effective density of the mass added to a particle during vapor growth.

Be aware that we can not validate the approach described above. There are not any published data of individual ice particle growth rates with variable temperature and supersaturation at $T < -40^{\circ}$ C to compare against. Under these conditions, it is unknown if a particle's deposition density or power-law exponent would change rapidly in response to a change in $s_{i,rat}$, or if they are set upon nucleation and early growth. Due to this limitation, we suggest utilizing the results from our wide range of constant experimental conditions as an approximation.

7. Summary and Discussion

We grew 268 individual ice particles with equivalent-mass spherical radii less than 40 μ m 635 inside the BEL diffusion chamber. Particle mass ratio time-series were measured at temperatures 636 between -65 and -40°C for supersaturations up to liquid saturation. Growth rates at high s_i typically 637 exceeded that of a solid sphere, which is consistent with complex crystal habits and can be treated 638 with an effective density. We estimated ρ_{eff} with model fits to the measured mass ratio time-series 639 by adjusting either a deposition density (ρ_{dep}) or a power-law exponent (P). Both ρ_{eff} models 640 represented the data well, and the time-averaged fit results resembled effective densities derived from models of budding rosettes and, at the largest growth rate ratios, columns. It is thus plausible 642 that many of the particles growing at high s_i developed those habits. The measured growth 643 enhancement due to such complexity was well characterized by a ratio of the supersaturation to its value at liquid saturation $(s_{i,rat})$. We have used 2-D relative frequency distributions of the ρ_{dep} 645 and P results to estimate the most frequent values of ρ_{dep} and P for any $s_{i,rat}$, which may then be 646 used to estimate a supersaturation-dependent effective density.

It is important to heed the limitations in our study. These particles grew under constant temperature and supersaturation, which is not the case in clouds. We have assumed that the particles with enhanced growth had deposition coefficients of unity, but due to the attachment kinetic effects required to produce complex ice habits, this cannot be true for the whole particle. Similarly, we treated particles with growth rate ratios less than unity as kinetics-limited, but facet development on a frozen droplet can also have anomalously low growth rates with a high particle-averaged α (Pokrifka et al. 2020; Harrington and Pokrifka 2021). Furthermore, while our analysis suggests

that many of the crystals we grew may have been budding rosettes or columns, we cannot confirm 655 the particle morphology. Our geometric model of a budding rosette, despite reproducing the vari-656 ability in the data, neglects facet hollowing, which likely occurred in our high- s_i experiments and 657 would contribute to the effective density reduction. Caution is therefore warranted in estimating growth rates from the budding rosette model, especially given its numerous required, but unknown, 659 parameters. The effective density parameterizations derived from the fits to the data with the de-660 position density and power-law exponent avoid these unknown parameters, but do so by avoiding a direct link to crystal geometry. That is, any and all complexity in particle shape is entangled in 662 ρ_{dep} and P. 663

Despite these limitations, our results are consistent with prior work. As shown in Fig. 5, our effective density estimates range from about 100 kg m⁻³ to ρ_i . This is comparable to estimates from prior laboratory studies, but most of those were from particles growing at $T \ge -22^{\circ}$ C and primarily near liquid saturation (high $s_{i,rat}$) (Fukuta 1969; Takahashi et al. 1991).

Prior effective density estimates under similar temperature and supersaturation conditions as in our experiments have been made from in-situ observations, and they also find that ρ_{eff} can be as low as 100 kg m⁻³, but for larger particles (Mitchell 1996; Heymsfield et al. 2004, 2007). Their effective density relations must be limited at some minimum diameter, generally between 70 and 100 μ m (Brown and Francis 1995; Heymsfield et al. 2010), otherwise nonphysical ice densities are produced. Smaller crystals are generally assumed to have the density of bulk ice ($\rho_{eff} \sim \rho_i$).

669

670

672

673

However, other effective density estimates derived from in-situ observations that accommodate 681 small particles are in good agreement with our measurements (Fig. 15). Figure 15 shows time-682 averaged effective densities as a function of growth rate ratio, much like the top panel of Fig. 5. 683 Here, the circles are derived from the power-law fits to the data, with shading indicating the 684 supersaturation ratio. Also plotted, in diamonds, are average effective densities following the mass-size parameterizations of Cotton et al. (2013), Erfani and Mitchell (2016), Fridlind et al. 686 (2016), and Lawson et al. (2019). In each case, we simulate the growth of a particle with an initial 687 radius of 10 μ m and a final mass ratio of 15 (final mass-equivalent spherical radius of ~ 25 μ m). The simulations use a temperature of -50°C and pressure of 970 hPa, and are across a range of 689 supersaturation ratios from 0 to 1, similar to the laboratory experiments. The observations of Cotton 690 et al. (2013) (cyan) are consistent with our data at low $s_{i,rat}$. Likewise, the rosette models of Fridlind

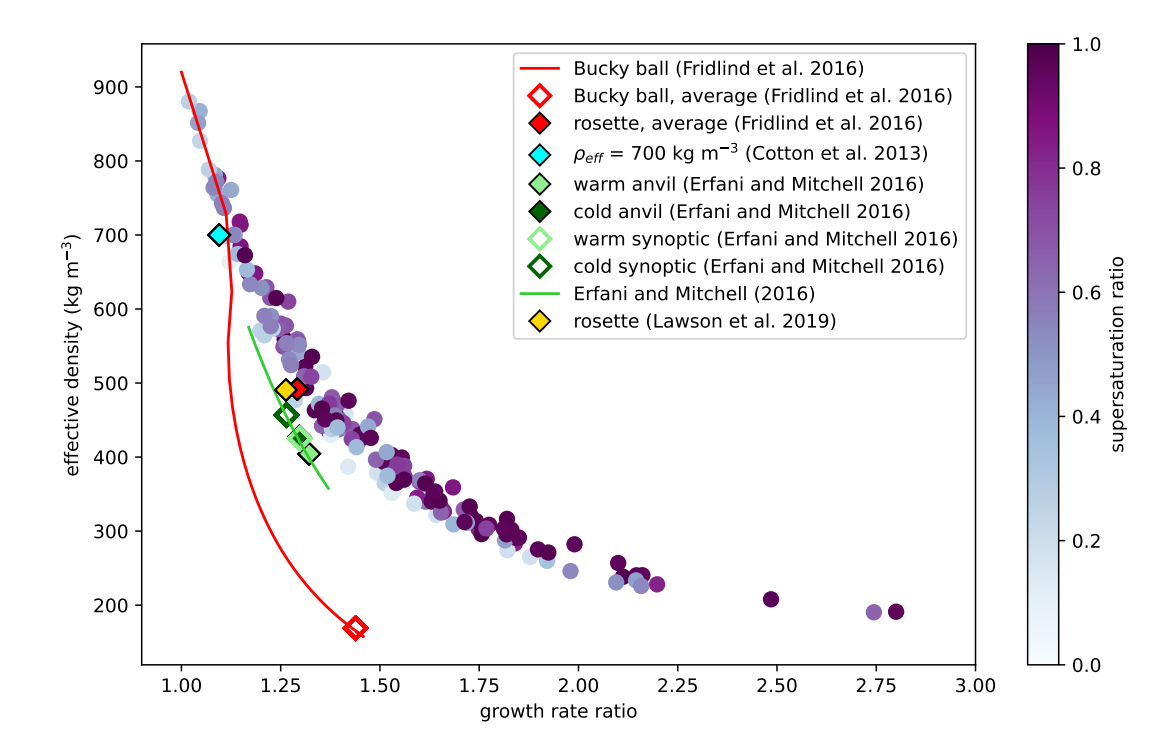


Fig. 15. Time-average effective density as a function of growth rate ratio. Circle are from the power-law fits to the mass ratio data, with darker shading indicating higher supersaturation ratio. Diamonds are from calculations using others' mass-size relationships. Shown in red are the rosette (solid diamond), Bucky ball (curve) and average of the Bucky ball (empty diamond) from Fridlind et al. (2016). The constant effective density from Cotton et al. (2013) is in cyan, and the rosette model from Lawson et al. (2019) is in yellow. Shown in green are the warm anvil (light solid), cold anvil (dark solid), warm synoptic (light empty), and cold synoptic (dark empty) cirrus cases from Erfani and Mitchell (2016), with the full growth range as a green curve.

et al. (2016) (solid red) and Lawson et al. (2019) (yellow) produce growth rate enhancements and effective density reductions that align well with the growth data. Erfani and Mitchell (2016) present multiple temperature-dependent mass-size relationships for synoptic (empty green) and anvil (solid green) cirrus. We have plotted the results from their warmest (light green) and coldest (dark green) cases, which produce slightly lower effective densities than our data, but they follow a similar functional form across our full mass range (green curve). The one outlier in this comparison is the Bucky ball model of Fridlind et al. (2016) (empty red). The average effective density from this model is significantly lower than the laboratory data. The full growth model across our mass range

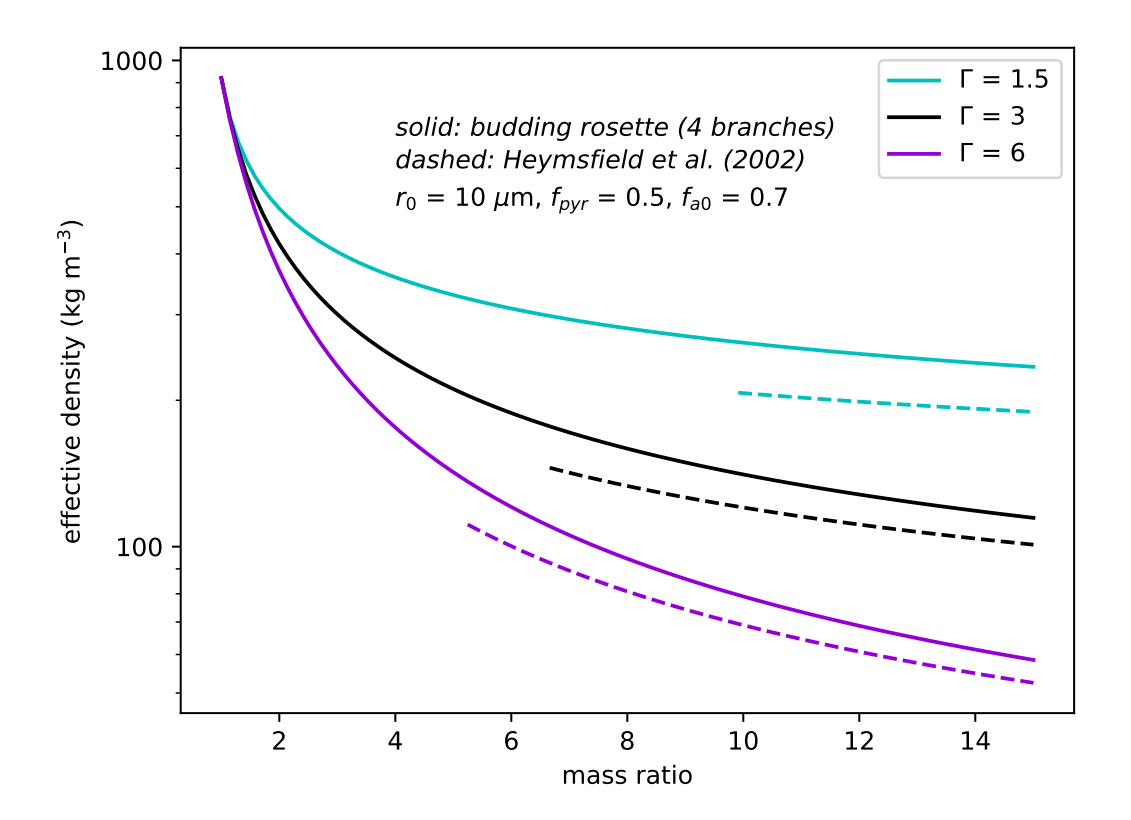


Fig. 16. Effective density from the budding rosette model with four branches (solid) compared to the geometric rosette model of Heymsfield et al. (2002) (dashed) as a function of mass ratio. The later model is limited to diameter $\geq 65 \ \mu m$ All simulations have an initial radius of $10 \ \mu m$, $f_{pyr} = 0.5$, and $f_{a0} = 0.7$. Cyan, black, and purple curves have Γ set to 1.5, 3.0, and 6.0, respectively. Note the logarithmic scale ρ_{eff} .

(red curve) reveals that, at small sizes, the Bucky ball model is an exceptional match to our data, but the effective density falls too quickly as the particle grows. Otherwise, these results indicate that particle growth rates produced by mass-size relationships derived from in-situ observations are corroborated by the growth rates of our laboratory measurements at low- to mid- $s_{i,rat}$. They do not, however, reach the highest growth rate ratios (and lowest effective densities) that our data and parameterizations produce at high- $s_{i,rat}$.

Further agreement between our study and in-situ observations appears in comparing geometric models. The correspondence between our measurements and our geometric model of a budding rosette indicates that a rosette model provides relatively accurate growth rates at high s_i . Heymsfield

et al. (2002) present a geometric rosette model suitable for larger crystals that was successfully used to interpret in-situ observations. Figure 16 shows that our model of a budding rosette, using four branches (solid curves), produces effective densities that approach the values from the model by Heymsfield et al. (2002) (dashed curves, beginning at a diameter of 65 μ m), when the particles grow larger (mass ratio $\gtrsim 10$). The overlaps in ρ_{eff} between both models, and between our budding rosette model and data, suggest that our measurement-derived effective density functions offer a plausible extension to nucleation sizes that is complementary to in-situ observations.

One advantage of our approach is that information on the time-dependence of growth is implicitly included in our parameterizations, since the mass-size relationships are derived from fits to the time-series data. Our measurement-derived parameterizations provide a method to model the growth of small ice particles that captures the effects of habit complexity.

- Acknowledgments. The comments of three anonymous reviewers are appreciated, as they have
- improved the quality of this manuscript. The authors are grateful for support through grants from
- the National Science Foundation (AGS-1824243 and AGS-2128347).
- Data availability statement. The laboratory data used in this manuscript is available through Data
- Commons, The Pennsylvania State University, at https://doi.org/10.26208/htw5-q166.

729 References

- Bacon, N., M. Baker, and B. Swanson, 2003: Initial stages in the morphological evolution of
- vapour-grown ice crystals: A laboratory investigation. Quart. J. Roy. Meteor. Soc., 129, 1903–
- ₇₃₂ 1927.
- Bailey, M., and J. Hallett, 2004: Growth rates and habits of ice crystals between -20 and -70°c. J.
- 734 Atmos. Sci., **61**, 514–544.
- Bailey, M., and J. Hallett, 2009: A comprehensive habit diagram for atmospheric ice crystals:
- Confirmation from laboratory, airs ii, and other field studies. *J. Atmos. Sci.*, **66**, 2888–2899.
- Baker, B., and R. P. Lawson, 2006: Improvement in determination of ice water content from
- two-dimensional particle imagery, part i: Image-to-mass relationships. Journal of Applied Me-
- teorology and Climatology, **45** (9), 1282 1290, https://doi.org/10.1175/JAM2398.1, URL
- https://journals.ametsoc.org/view/journals/apme/45/9/jam2398.1.xml.
- Brandes, E., K. Ikeda, G. Zhang, M. Schönhuber, and R. Rasmussen, 2007: A statistical and phys-
- ical description of hydrometeor distributions in colorado snowstorms using a video disdrometer.
- Journal of Applied Meteorology and Climatology, **46** (**5**), 634–650.
- Brown, P., and P. Francis, 1995: Improved measurements of the ice water content in cirrus using a
- total-water probe. *J. Atmos. Ocean. Tech.*, **12**, 410–414.
- Chen, J.-P., and D. Lamb, 1994: The theoretical basis for the parameterization of ice crystal habits:
- Growth by vapor deposition. *J. Atmos. Sci.*, **51**, 1206–1221.
- Chen, J.-P., and T.-C. Tsai, 2016: Triple-moment modal parameterization for the adaptive growth
- habit of pristine ice crystals. J. Atmos. Sci., 73, 2105–2122.

- Chiruta, M., and P. Wang, 2003: The capacitance of rosette ice crystals. J. Atmos. Sci., 60, 836–846.
- Cotton, R., and Coauthors, 2013: The effective density of small ice particles obtained from in situ 751 aircraft observations of mid-latitude cirrus. Quart. J. Roy. Meteor. Soc., 139, 1923–1934. 752
- Davis, E., 2010: A button electrode levitation chamber for the study of ice crystal growth under atmospheric conditions. M.S. thesis, Meteorology, The Pennsylvania State University, University 754 Park PA, 16801, USA. 755
- Dunnavan, E. L., and Z. Jiang, 2019: A general method for estimating bulk 2D projections of ice 756 particle shape: Theory and applications. J. Atmos. Sci., 76, 305–332. 757
- Dunnavan, E. L., Z. Jiang, J. Y. Harrington, J. Verlinde, K. Fitch, and T. J. Garrett, 2019: The 758 shape and density evolution of snow aggregates. J. Atmos. Sci., 76, 3919–3940. 759
- Elliott, W. J., 1971: Dimensions of thermal diffusion chambers. J. Atmos. Sci., 28, 810–811.
- Erfani, E., and D. L. Mitchell, 2016: Developing and bounding ice particle mass- and areadimension expressions for use in atmospheric models and remote sensing. Atmospheric Chem-762 istry and Physics, **16** (**7**), 4379–4400. 763
- Frank, F. C., 1982: Snow crystals. Contemporary Physics, 23 (1), 3–22, https://doi.org/10.1080/ 00107518208231565. 765
- Fridlind, A. M., R. Atlas, v. D. Bastiaan, J. Um, G. M. McFarquhar, A. S. Ackerman, E. J. Moyer, 766 and R. P. Lawson, 2016: Derivation of physical and optical properties of mid-latitude cirrus 767 ice crystals for a size-resolved cloud microphysics model. Atmospheric Chemistry and Physics, **16** (**11**), 7251–7283. 769
- Fukuta, N., 1969: Experimental studies on the growth of small ice crystals. *Journal of Atmospheric* 770 Sciences, **26** (3), 522 – 531, https://doi.org/10.1175/1520-0469(1969)026(0522:ESOTGO)2. 771
- 0.CO;2, URL https://journals.ametsoc.org/view/journals/atsc/26/3/1520-0469_1969_026_0522_ 772 esotgo_2_0_co_2.xml.

Fukuta, N., and T. Takahashi, 1999: The growth of atmospheric ice crystals: A summary of 774 findings in vertical supercooled cloud tunnel studies. J. Atmos. Sci., **56**, 1963–1979.

- Garrett, T. J., S. E. Yuter, C. Fallgatter, K. Shukurko, S. R. Rhodes, and J. L. Endries, 2015:
- Orientations and aspect ratios of falling snow. *Geophys. Res. Let.*, **42**, 4617–4622, https://doi.org/
- https://doi.org/10.1002/2015GL.
- Harrington, J., and G. Pokrifka, 2021: Approximate models for lateral growth on ice crystal surfaces during vapor depositional growth. *J. Atmos. Sci.*, **78**, 967–981.
- Harrington, J. Y., A. Moyle, L. E. Hanson, and H. Morrison, 2019: On calculating deposition coefficients and aspect-ratio evolution in approximate models of ice crystal vapor growth. *Journal* of the Atmospheric Sciences, **76** (6), 1609–1625, https://doi.org/10.1175/JAS-D-18-0319.1.
- Harrison, A., A. Moyle, M. Hanson, and J. Harrington, 2016: Levitation diffusion chamber measurements of the mass growth of small ice crystals from vapor. *J. Atmos. Sci.*, **73**, 2743–2758.
- Hashino, T., and G. J. Tripoli, 2007: The spectral ice habit prediction system (SHIPS). Part I: Model description and simulation of the vapor deposition process. *J. Atmos. Sci.*, **64**, 2210–2237.
- Hashino, T., and G. J. Tripoli, 2008: The spectral ice habit prediction system (SHIPS) Part II:

 Simulation of nucleation and depositional growth of polycrystals. *J. Atmos. Sci.*, **65**, 3071–3094.
- Heymsfield, A., A. Bansemer, C. Schmitt, C. Twohy, and M. Poellot, 2004: Effective ice particle densities derived from aircraft data. *J. Atmos. Sci.*, **61**, 982–1003.
- Heymsfield, A., A. Bansemer, and C. H. Twohy, 2007: Refinements to ice particle mass dimensional and terminal velocity relationships for ice clouds. Part I: Temperature dependence. *J. Atmos. Sci.*, **64**, 1047–1067.
- Heymsfield, A., and J. Iaquinta, 2000: Cirrus crystal terminal fall velocities. *J. Atmos. Sci.*, **57**, 916–938.
- Heymsfield, A., S. Lewis, A. Bansemer, J. Iaquinta, L. Miloshevich, M. Kajikawa, C. Twohy, and
 M. Poellot, 2002: A general approach for deriving the properties of cirrus and stratiform ice
 cloud particles. *J. Atmos. Sci.*, **59**, 3–29.
- Heymsfield, A., C. Schmitt, and A. Bansemer, 2010: Improved representation of ice-particle masses based on observations in natural clouds. *J. Atmos. Sci.*, **67**, 3303–3318.

- Jensen, A., J. Harrington, H. Morrison, and J. Milbrandt, 2017: Predicting ice shape evolution in a bulk microphysics model. *J. Atmos. Sci.*, **74**, 2081–2104.
- Lawson, R. P., and Coauthors, 2019: A review of ice particle shapes in cirrus formed in situ and in anvils. *J. Geophys. Res.*, **124**, https://doi.org/https://doi.org/10.1029/2018JD030122.
- Leinonen, J., J. Grazioli, and A. Berne, 2021: Reconstruction of the mass and geometry of snow-
- fall particles from multi-angle snowflake camera (MASC) images. Atmospheric Measurement
- Techniques, **14** (**10**), 6851–6866.
- Magee, N., and Coauthors, 2021: Captured cirrus ice particles in high definition. *Atmos. Chem.*Phys., 21, 7171–7185.
- Matsuo, T., and N. Fukuta, 1987: Experimental study of ice crystal growth below water saturation in the university of utah supercooled cloud tunnel. *Papers in Meteorology and Geophysics*, **38 (4)**, 247–264, https://doi.org/10.2467/mripapers.38.247.
- Mitchell, D. L., 1996: Use of mass- and area-dimensional power laws for determining precipitation particle terminal velocities. *J. Atmos. Sci.*, **53**, 1710–1723.
- Morrison, H., and J. A. Milbrandt, 2015: Parameterization of ice microphysics based on the prediction of bulk particle properties. part i: Scheme description and idealized tests. *J. Atmos.*Sci., 72, 287–311.
- Muramoto, K., K. Matsuura, and T. Shiina, 1995: Measuring the density of snow particles and snowfall rate. *Electron. Comm. Jpn. Pt. III*, **78**, 71–79.
- Nelson, J., 1994: A Theoretical Study of Ice Crystal Growth in the Atmosphere. Ph.D. thesis,
 University of Washington, 183pp.
- Nelson, J., 2001: Growth mechanisms to explain the primary and secondary habits pf snow crystals.

 Philos. Mag. A., **81, 2337–2373.
- Nelson, J., and M. Baker, 1996: New theoretical framework for studies of vapor growth and sublimation of small ice crystals in the atmosphere. *J. Geophys. Res.*, **101**, 7033–7047.
- Nelson, J., and C. Knight, 1998: Snow crystal habit changes explained by layer nucleation. *J. Atmos. Sci.*, **55**, 1452–1465.

- Nelson, J., and B. Swanson, 2019: Air pockets and secondary habits in ice from lateral-type growth. *Atmospheric Chemistry and Physics Discussions*, **2019**, 1–51, https://doi.org/10.5194/acp-2019-280.
- Parungo, F., and H. Weickmann, 1973: Growth of ice crystals from frozen droplets. *Meteor. Atmos.*Phys., **46**, 289–304.
- Pokrifka, G. F., A. M. Moyle, L. E. Hanson, and J. Y. Harrington, 2020: Estimating surface attachment kinetic and growth transition influences on vapor-grown ice crystals. *Journal of the Atmospheric Sciences*, **77** (7), 2393 2410, https://doi.org/10.1175/JAS-D-19-0303.1, URL https://journals.ametsoc.org/view/journals/atsc/77/7/jasD190303.xml.
- Rees, K. N., D. K. Singh, E. R. Pardyjak, and T. J. Garrett, 2021: Mass and density of individual frozen hydrometeors. *Atmospheric Chemistry and Physics*, **21** (**18**), 14 235–14 250.
- Reisner, J., R. M. Rasmussen, and R. T. Bruintjes, 1998: Explicit forecasting of supercooled liquid water in winter storms using the mm5 mesoscale model. *J. Atmos. Sci.*, **124**, 1071–1107.
- Ryan, B. F., E. R. Wishart, and E. W. Holroyd, 1974: The densities and growth rates of ice crystals between -5°C and -9°C. *Journal of Atmospheric Sciences*, **31** (**8**), 2136 2141, https://doi.org/10. 1175/1520-0469(1974)031\(\rangle 2136:TDAGRO\)\(\rangle 2.0.CO; 2, URL https://journals.ametsoc.org/view/journals/atsc/31/8/1520-0469_1974_031_2136_tdagro_2_0_co_2.xml.
- Ryan, B. F., E. R. Wishart, and D. Shaw, 1976: The growth rates and densities of ice crystals between -3°C and -21°C. *J. Atmos. Sci.*, **33** (**5**), 842–850.
- Skrotzki, J., and Coauthors, 2013: The accommodation coefficient of water molecules on ice cirrus cloud studies at the AIDA simulation chamber. *Atmos. Chem. Phys.*, **13**, 4451–4466.
- Takahashi, T., T. Endoh, G. Wakahama, and N. Fukuta, 1991: Vapor diffusional growth of free-falling snow crystals between -3 and -23°c. *J. Meteorol. Soc. Japan*, **69**, 15–30.
- Takahashi, T., and N. Fukuta, 1988: Supercooled cloud tunnel studies on the growth of snow crystals between-4 and-20°C. *Journal of the Meteorological Society of Japan. Ser. II*, **66** (6), 841–855, https://doi.org/10.2151/jmsj1965.66.6_841.

- Um, J., and G. M. McFarquhar, 2011: Dependence of the single-scattering properties of small ice crystals on idealized shape models. *Atmospheric Chemistry and Physics*, **11** (**7**), 3159–3171, https://doi.org/10.5194/acp-11-3159-2011, URL https://acp.copernicus.org/articles/11/3159/2011/.
- Weitzel, M., S. K. Mitra, M. Szakáll, J. P. Fugal, and S. Borrmann, 2020: Application of holography
 and automated image processing for laboratory experiments on mass and fall speed of small
 cloud ice crystals. *Atmospheric Chemistry and Physics*, 20 (23), 14 889–14 901, https://doi.org/
 10.5194/acp-20-14889-2020, URL https://acp.copernicus.org/articles/20/14889/2020/.
- Westbrook, C. D., R. J. Hogan, and A. J. Illingworth, 2008: The capacitance of pristine ice crystals
 and aggregate snowflakes. *J. Atmos. Sci.*, 65, 206–219.
- Wood, S., M. Baker, and D. Calhoun, 2001: New model for the vapor growth of hexagonal ice crystals in the atmosphere. *J. Geophys. Res.*, **106**, 4845–4870.
- Zhang, C., and J. Harrington, 2014: Including surface kinetic effects in simple models of ice vapor diffusion. *J. Atmos. Sci.*, **71**, 372–390.